Design and Performance Evaluation of a Battery Simulator

by

Haoduo Wang

A thesis
presented to the University of Waterloo
in fulfillment of the
thesis requirement for the degree of
Master of Applied Science
in
Electrical and Computer Engineering

Waterloo, Ontario, Canada, 2016

AUTHOR'S DECLARATION

I hereby declare that I am the sole author of this thesis. This is a true copy of the thesis, including any required final revisions, as accepted by my examiners.

I understand that my thesis may be made electronically available to the public.

Abstract

The increasing demand on alternative fuel vehicles, especially electric vehicles (EVs), has created an enormous market, as well as great opportunities for further improvements, for battery industry. However, using battery packs as the energy source in the design/development process of new electric vehicles, is not an optimal choice, due to high cost and cycle life reduction of battery cells. Utilizing a battery simulator, with bidirectional power transactions with the grid, which can emulate different battery cell chemistries and battery pack sizes, is a viable solution to the problem.

In this work, a battery simulator is proposed which has the potential of providing a high power DC supply, while emulating multiple types of battery cell chemistries, including Li-ion, lead-acid, NiCd, NiMH, and polymer-lithium. The proposed battery simulator consists of two main parts. The first part is the battery model that generates the reference signal for the DC terminal voltage of the battery simulator according to the present value of the load current. The second part is a voltage-source converter (VSC) that controls its DC-side voltage according to the reference signal provided by the battery model. Different battery modelling approaches are introduced and compared to select the most appropriate model to be realized. The control strategy and controller tuning method are also discussed following a systematic approach. Simulations under various loading conditions are carried out and extended simulation results are presented to verify the expected capabilities of the proposed battery simulator.

Acknowledgements

I would like to express my greatest gratitude to my supervisor Professor Mehrdad Kazerani for his unreserved help during the research. This thesis could never been completed without his continuous and generous support. His strict attitude, profound knowledge and humble manner are always the example for me.

I deeply appreciate my parents and Xueling for their ceaseless support and love. Your words were always the best remedy for stress and the weekly talking enlightened my path.

I owe gratitude to Zuher. Whenever I encountered technical issues, you were always good to discuss with. I also owe gratitude to Mahmoud and Marten for their help in lab.

To all others in the group, I feel honored to work with you guys. Thank you.

Table of Contents

List of Figures

List of Tables

Chapter 1
Introduction

1.1 Motivation

With increasing public demand for limiting contributions from transportation, which is the primary sector, to the greenhouse gas emissions, electrical vehicles (EVs), hybrid electric vehicles (HEVs) and plug-in hybrid electric vehicles (PHEVs) are gaining a larger share in the vehicle market. Such trend stimulates manufacturers to develop new high-performance and environment-friendly products with low or even zero emissions. In past eight years, as a newly emerging company, Tesla Motors, has created 3 all-electric cars known as Tesla Roadster, Tesla Model S and Tesla Model X. Meanwhile, the traditional car manufacturers have started to follow the trend to remain in the game. For instance, Nissan launched its all-electric car Leaf in 2011, while BMW unveiled i3 later in 2013.

The estimation made by Electrical Vehicle Initiative (EVI) shows that by 2020 the global EV stock would increase to 20 million from 180,000, at the end of 2012 [1]. Figure 1-1 gives a visual impression of this expected growth.

Figure 1-1 Estimated EV Stock by 2020[1]

To achieve the 20 million EVs goal by 2020, large numbers of new models would be developed and manufactured which will dramatically raise the demand for the battery packs to provide DC energy sources. However, during the developing and testing process for new vehicle models, using actual battery packs is not the optimal choice, as the high cost and capacity fading of battery cells will boost the price further.

In order to reduce the cost, especially during the development and testing stage, a battery simulator/emulator with the full capability of the real battery pack and the same input and output characteristics is to be used. A high-performance battery simulator interacts with the grid to (i) absorb power from the grid and provide power to the load connected to its output terminals, and (ii) deliver the power absorbed from the load to the grid. A battery simulator can simulate behaviors of various types of battery cell chemistries and can last much longer than a battery pack, at reduced initial and operating costs.

1.2 Performance Gaps Identified in the Existing Battery Simulators

A large number of battery simulators occupy the market. However, few satisfy the expected experimental requirements as a power supply. A huge gap exists between the request for battery simulators which could power the electric powertrains of EVs and the products in stock. A literature review and a background overview related to battery simulator design are presented in Chapter 2. The major drawbacks are as follows.

a. The majority of products' power level is below 10 kW [5][6][7] which is far below the power supply requirement for vehicles. For instance, Nissan Leaf's battery pack drives an 80 kW permanent-magnet synchronous motor [2], while Tesla Roadster's peak power could be up to 215 kW [3].

b. Few products in stock could emulate characteristics of different types of battery cells, even though types of battery cells used in battery packs of vehicles vary according to the energy storage system. Lithium-ion battery, which has a high power-to-weight ratio, high energy efficiency, good high-temperature performance, and low self-discharge, is the most popular choice for EVs and PHEVs, while nickel-metal cell is widely used in HEVs for its long cycle life and high abuse tolerance. Lead-acid battery is usually applied for auxiliary loads [4].

c. Most existing battery simulators have narrow output voltage ranges and small current limits which limit the adaptability of the simulator.

d. The cost would be very high if multiple modules of smaller size simulators are used to satisfy high power levels or if purchase the customized high power battery simulator. The following two examples are given to get an idea of $/kW cost of having an 80kW battery simulator based on the equipment available on the market.

   Example 1: If the DLM 20-30 DC Supply modules, each rated at 600 W [5], are used to drive the 80kW Nissan Leaf's powertrain, at least 134 simulator modules are required. With price of each 600W module being $ 1,923 [5], which is equivalent to 3,205 $/kW, the overall cost of an 80kW battery simulator becomes approximately $ 258,000, which is considered very high.

   Example 2: If the -170kW to +125kW, -640A to +530A, 8-420V, DC ABC-170 Dual Channel Test System by AeroVironment is considered, the total cost will be approximately $210,000 and the per unit cost will be approximately 1,235 $/kW, which is smaller than the previous case, but still very high.

1.3 Estimation of Initial Cost of Creating a New Battery Simulator

The equipment used for a battery simulator can be divided into three parts: (i) An IGBT three-phase converter; (ii) a microcontroller that generates switching signals according to the implemented codes;

and (iii) sensors that detect voltage/current values from both ac and dc sides of VSC and send voltage/current signals to microcontroller.

To drive Nisan Leaf's 80 kW synchronous motor, 3 modules of the Powerex CM100MXA-24S three-phase IGBT module, which has the maximum collector-emitter voltage of 1200 V and maximum collector current of 100 A, is used as an example to estimate the cost. The unit price of the module given by Digi-Key is presently $155.67. It was reported the bill of materials for the sensors and microcontroller adapter board [35] for creating a microgrid test bed, which is presented in Table 1-1.

Table 1-1 Costs for Materials

Part	Cost (CAD)
Three-phase voltage sensor	193.41
Three-phase current sensor	3×119.85
DC voltage and current sensors	2×115.53
Microcontroller adaptor board and Controller	411.27
DC Capacitor	54.8
IGBT Gate Drivers	3×210
Gate Drivers' DC Power Supplies	3×335
AC Inductors	3×≅100
Protection	3×141

Therefore, the cost of the material for the hardware plus the cost for one Master's student over the period of 16 months (scholarships and subsidies are included), which is approximately $22,600, is approximately $26,600. This implies a cost of approximately $246/kW.

Hence, comparing the per unit costs (in $/kW) of the battery simulator on the market and the one proposed in this work, a considerable reduction in the cost can be obtained. Having said this, one should note that the products on the market are professionally made and packaged and are meant for industrial use, whereas the prototype in the lab is made by graduate students and cannot compete in performance and reliability.

1.4 Research Objectives

In order to overcome the shortcomings of the existing battery simulators, new equipment which could emulate different kinds of battery cells to provide a high-power supply to the motor drive system, while being capable of adapting to different voltage and current requirements, has to be designed. Therefore, the mission of the research could be divided into the following three main parts.

a. Find a reasonable battery model, which accurately reproduces input and output characteristics of different cell types, to work as the reference signal for the power electronic converter part;

b. Have a systematic design for VSC, allowing power transactions with the grid and making the battery simulator output voltage to follow the reference signal produced by the battery model; and

c. Choose a reasonable load to test the battery simulator design.

1.5 Structure of the Thesis

The thesis consists of 5 chapters and 2 appendices. Chapter 1 gives a general description of the motivations for the research, performance gaps identified in the existing battery simulators and research objectives. Chapter 2 provides the background on the battery models and voltage-source converter (VSC) which acts as the foundation for the proposed battery simulator in the next chapters. Surveys for different modeling methods for battery cells are described and compared. Discussion about the modeling of VSC is also presented. Chapter 3 presents the details of the battery simulator which satisfies the requirement for the power supply in the experimental process for developing electric-drive vehicle. The design process is explained including the creation of the circuitry to emulate the performance of real battery cells, generation of control loop and the derivation of transfer function for VSC. Chapter 4 unveils the battery emulator system's performance under different load conditions which proves the effectiveness of the proposed system and its adaptability. Chapter 5 concludes the thesis and looks ahead for future work. Appendix A presents the Matlab Code for the

study of the stability of VSC. Appendix B gives the C code for a block in the simulation which simplifies the battery circuit. Appendix C provides information on typical Type I and Type II control systems. The information presented in Appendix C will be directly used in the design process of VSC in chapter 3.

Chapter 2

Background Overview

2.1 Study of Battery Model

A wide variety of battery models with varying degrees of complexity have been developed by researchers around the world. They capture battery behavior for specific purposes, from battery design and performance estimation to circuit simulation [8].

The models developed can be divided roughly into 3 types: empirical models, physical models and abstract models. Standards, including accuracy, computational complexity, configuration effort and analytical insight, are proposed to judge the validation of the models created [9]. The following figure shows the classification of battery models.

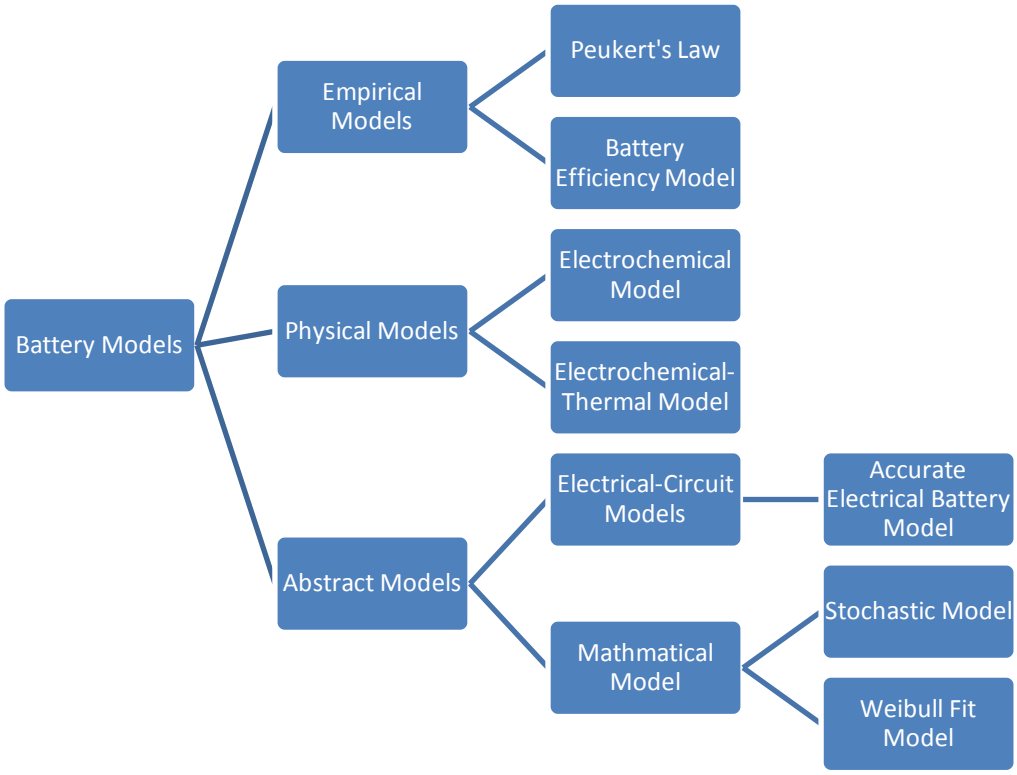

Figure 2-1 Classification of Battery Models

2.1.1 Empirical Model

Empirical Models have the simplest configuration due to the theory behind such models. Empirical values gained by direct or indirect observation are quantified to create non-physically-significant equations to describe the characteristics of battery and predict its future performance. Although such models work in certain circumstances, lacking physical meaning hugely affects the accuracy if parameters change, and limits their analytical insight [9].

2.1.1.1 Peukert's Law

The German scientist Wilhelm Peukert was the first to present the description for lead-acid battery in 1897. For a one-ampere discharge rate, Peukert's law is stated as

$$C_p = I^k t \tag{2-1}$$

where

C_p is the capacity (in Ah) at a one-ampere discharge rate,

I is the discharge current (in amperes),

t is the time (in hours) to discharge the battery, and

k is the Peukert constant.

For practical use, the law can also be presented as

$$t = H(\frac{C}{IH})^k \tag{2-2}$$

where

H is the rated discharge time (in hours),

C is the rated capacity at that discharge rate (in ampere-hours),

I is the actual discharge current (in amperes),

K is the dimensionless Peukert constant, and

t is the actual time to discharge the battery (in hours).

From the above equations, we could easily conclude that Peukert's law could only describe battery performance with constant load which largely limits its application.

2.1.1.2 Battery Efficiency Model

The battery efficiency which is defined as the ratio of real capacity to the theoretical was modeled as linear quadratic function of load current by M. Pedram and Q. Wu [10]. They focused on the study of the creation of battery model as well as how to extend battery life time. They claimed in their paper that a uniformly distributed current could jeopardize the life span of battery most, while a constant current would do the least harm.

Such model could withstand variable load current and its applications are mainly in maximizing multi-battery system's lifetime [14], and minimizing the discharge-delay product in an interleaved dual-battery system design [9][15].

2.1.2 Physical Model

Physical models characterize the fundamental mechanism of power generation and relate battery design parameters to microscopic information [8]. Such models have the best accuracy in describing the working process of battery cells and providing parameter values including current, voltage, and capacity. However, these models suffer the slowest computation process, as the most complex algorithms and the hardest configuration, compared with other two model types, are required due to the proprietary nature of the method. Electrochemical models, in most cases, are used in optimizing the battery's physical design.

2.1.2.1 Electrochemical Model

Based on J.S. Newman's concept [21], the further developed electrochemical model was proposed by D. Dees, V. Battaglia and A. Belanger [16], in which mass, energy, and momentum transport of each species for each phase and component of the cell were taken into consideration. Such model is able to predict macroscopic values like cell voltage and current, as well as calculate microscopic quantities such as potential, local distribution of concentration, and inside temperature.

2.1.2.2 Electrochemical-Thermal Model

L. Song and J. Evans proposed a coupled electrochemical-thermal model to study physical process for lithium battery, in which detailed information, such as cell voltage, current distribution, reaction rate,

and heat generation rate at different positions in the battery stack can be calculated [17]. The calculation structure of the model is shown in Figure 2-2.

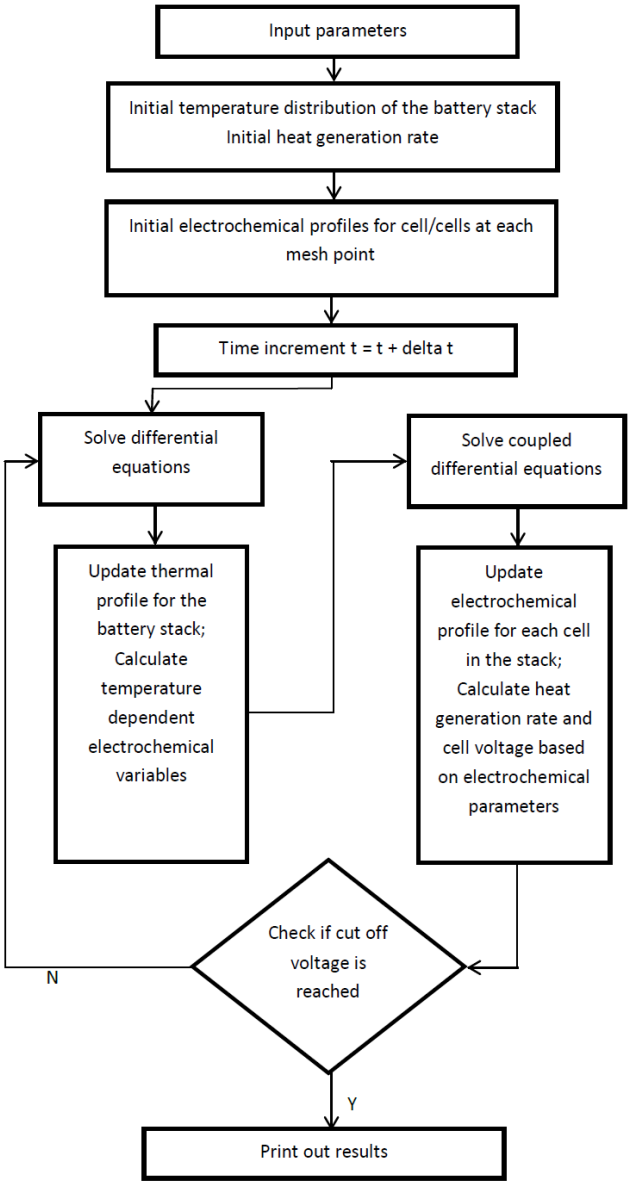

Figure 2-2 Calculation Process [17]

2.1.3 Abstract Models

2.1.3.1 Electrical-Circuit Model

Researchers use electrical components including capacitors, inductors, and resistors to simulate the behavior of battery cell both in transient state and steady state. Different criterions are applied and developed to make a compromise between the requirements of accuracy and the ease of computation. Generally, three basic models could be mentioned, i.e., Thevenin-based model, Impedance-based model and Runtime-based model. Comparison of the three models has been made by M. Chen and G. Rincon-Mora [8], as shown in Table 2-1.

Table 2-1 Comparison of three Basic Models

Predicting Capability	Thevenin-Based Model	Impedance-Based Model	Runtime-Based Model
DC	No	No	Yes
AC	Limited	Yes	No
Transient	Yes	Limited	Limited
Battery Runtime	No	No	Yes

Based on the three basic models, M. Chen and G. Rincon-Mora propose the Accurate Electrical Battery model [8] which consists of a capacitor, a current-controlled voltage source (CCVS) which represents the usable capacity, runtime and SoC of the battery, a series resistance which represents the steady state response, an R-C network which represents the long-term and short term transient responses, and a parallel resistance which represents the self-discharge or fading effect of the cell. The self-discharge resistor is a function of temperature and SoC. The model is shown in Figure 2-3.

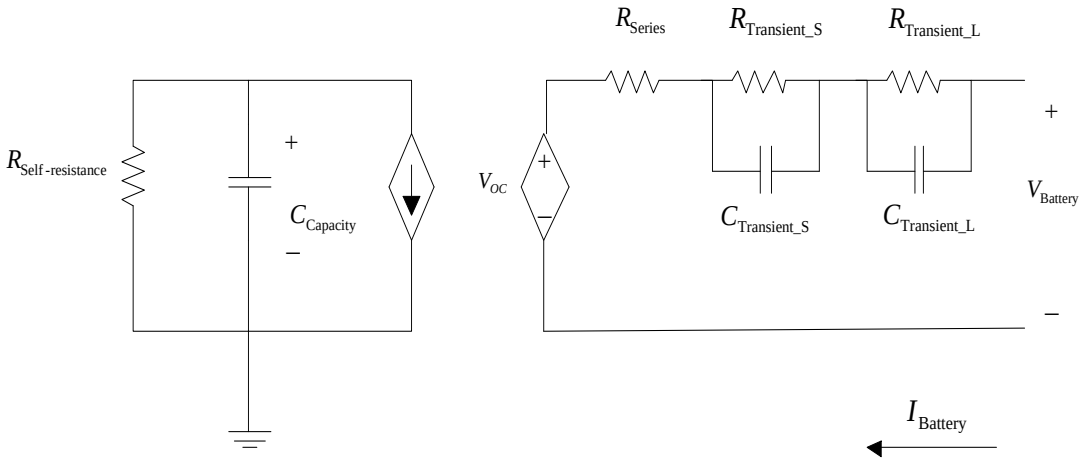

Figure 2-3 Accurate Electrical Battery Model [8]

The usable capacity of the battery can be modeled by equation (2-3) as a full-capacity capacitor, a self-discharge resistor and an equivalent series resistor which is sum of the steady state resistor R_{Series}, the short term transient resistor $R_{Transient-S}$, and the long-term transient $R_{Transient-L}$.

$$C_{Capacity} = 3600 \cdot Capacity \cdot f_1(Cycle) \cdot f_2(Temp) \tag{2-3}$$

where

$C_{Capacity}$ is the whole charge stored in the battery (in coulomb),

$Capacity$ is the nominal capacity of the battery (in Ah),

$f_1(Cycle)$ is a cycle number-dependent correction factor, and

$f_2(Temp)$ is a temperature-dependent correction factor.

The battery cell is initialized at 0% or 100% by putting $C_{Capacity}$ equal to 0 or 1. Some simplification has been made by setting $f_1(Cycle)$ and $f_2(Temp)$ to 1.

The open circuit voltage is written as a function of SoC as

$$V_{OC}(SoC) = -1.031e^{-35SoC} + 3.685 + 0.2156SoC - 0.1178SoC^2 + 0.3201SoC^3 \tag{2-4}$$

Steady state series resistance is written as a function of SoC as

$$R_{\text{series}}(SoC) = 0.1562e^{-24.37SoC} + 0.07446 \tag{2-5}$$

Long-term transient resistance is written as a function of SoC as

$$R_{\text{Transient\_L}}(SoC) = 6.603e^{-155.2SoC} + 0.04984 \tag{2-6}$$

Long-term transient capacitance is written as a function of SoC as

$$C_{\text{Transient\_L}}(SoC) = -6056e^{-27.12SoC} + 4475 \tag{2-7}$$

Short-term transient resistance is written as a function of SoC as

$$R_{\text{Transient\_S}}(SoC) = 0.3208e^{-29.14SoC} + 0.04669 \tag{2-8}$$

Short-term transient capacitance is written as a function of SoC as

$$C_{\text{Transient\_S}}(SoC) = -752.9e^{-13.51SoC} + 703.6 \tag{2-9}$$

The model given by equations (2-4)-(2-9) is created based on the 850 mAh TCL PL-383562 polymer Li-ion battery. Different parameters should be applied according to the specific types of battery chemistries.

2.1.3.2 Mathematical Model

Statistical approach was developed by K. Syracuse and W. Clark [12]. They recorded voltage values under different discharge stages, while keeping load and temperature constant. Weibull model with specific coefficients were used to represent voltage as a function of delivered capacity or charge lost [9]. Response surface methodology was used for creating point estimates for average running voltage and capacity. The same method was also applied to predict cell's longevity.

C. Chiasserini and R. Rao used [25] used a stochastic model in which the charge recovery process was described as a decreasing exponential functions of discharged Capacity and SoC. Though largely simplified when compared with the electrochemical model, the pure math model could successfully capture the fundamental behavior of the battery cell. However, since only charge recovery process was taken into consideration, other battery nonlinearities could not be represented [9].

2.1.4 Comparison of Presented Battery Models

R. Rao and D. Rakhamatov [9] compared different types of models. Their analysis is given in Table 2-2.

Table 2-2 Comparison of Battery Models [9]

	Model Type	Temperature Effect	Capacity Fading	Accuracy	Computational Complexity	Configuration Effort	Analytical Insight
Peukert's Law	Empirical Model	Yes (Recalibration in each temperature stage)	No	Medium	Low	Low	Low
Battery Efficiency Model	Empirical Model	Yes (Recalibration in each temperature stage)	No	Medium	Low	Low	Low
Electrochemical Model/ Electrochemical-Thermal Model	Physical Model	Yes	Yes	Very high	High	Very high	Low
Electrical-Circuit Models	Abstract Model	Yes	Yes	Medium	Medium	Medium	Medium
Mathematical Models	Abstract Model	Yes	No	Medium	Above Medium	Low	Medium

2.2 Study of VSC

Voltage-source converter (VSC) plays a key role in the battery simulator, as it controls the terminal voltage of the battery simulator at any load current level according to the battery model. The grid connection allows bidirectional power flow to and from the load, as in an actual battery. In this section, a literature review for VSC will be performed that will include mathematical modeling of VSC both in abc and dq frames, the stability study and the decoupling method.

2.2.1 Modelling of VSC in abc Frame

In this section, the general mathematical model (small-signal model) for VSC would be derived which can be utilized in the stability study of VSC. The circuit diagram of VSC is shown in Figure 2-4.

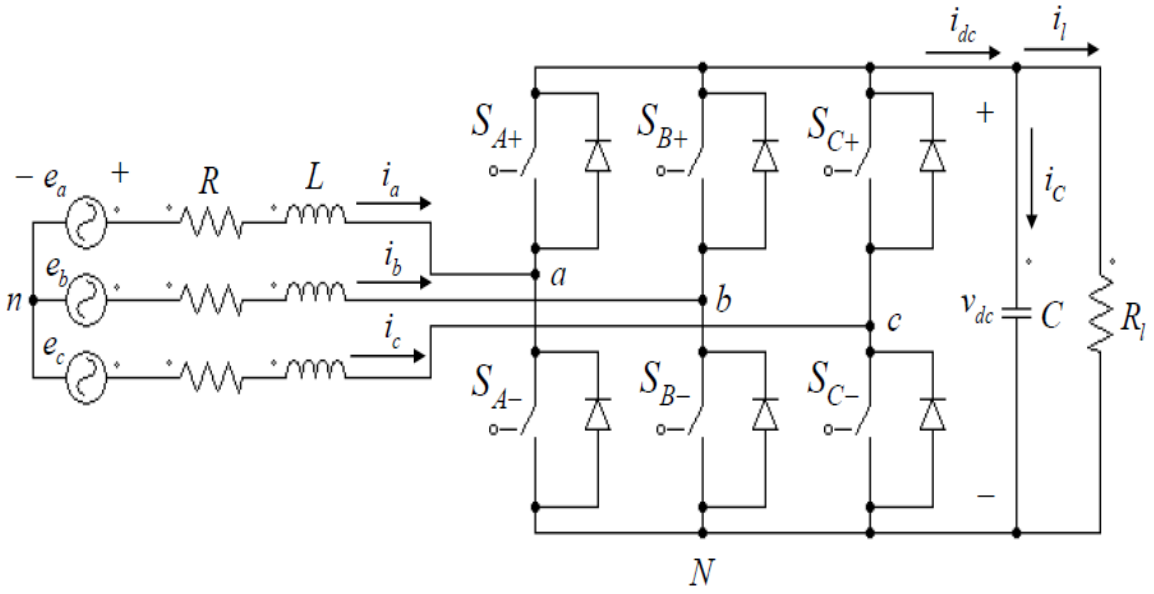

Figure 2-4 Circuit diagram of VSC

It should be noted that when S_{A+} is on, S_{A-} is off. The same situation applies to S_B and S_C. Therefore, the switching function of VSC can be expressed as

$$\begin{cases} S_A = \begin{cases} 1 \rightarrow S_{A+}\ ON \\ 0 \rightarrow S_{A-}\ ON \end{cases} \\ S_B = \begin{cases} 1 \rightarrow S_{B+}\ ON \\ 0 \rightarrow S_{B-}\ ON \end{cases} \\ S_C = \begin{cases} 1 \rightarrow S_{C+}\ ON \\ 0 \rightarrow S_{C-}\ ON \end{cases} \end{cases} \tag{2-10}$$

The relationship between the voltage at the dc side, v_{dc}, and the ac-side phase voltages with respect to point N is

$$\begin{cases} V_{aN} = S_A v_{dc} \\ V_{bN} = S_B v_{dc} \\ V_{cN} = S_{VC} v_{dc} \end{cases} \tag{2-11}$$

The current on the dc side is

$$i_{dc} = S_A \cdot i_a + S_B \cdot i_b + S_C \cdot i_c \tag{2-12}$$

According to KVL, it can be found that

$$\begin{cases} e_a = Ri_a + L\dfrac{di_a}{dt} + v_{aN} + v_{Nn} \\ e_b = Ri_b + L\dfrac{di_b}{dt} + v_{bN} + v_{Nn} \\ e_c = Ri_c + L\dfrac{di_c}{dt} + v_{cN} + v_{Nn} \end{cases} \tag{2-13}$$

Also, according to KCL, one can write

$$i_{dc} = C\frac{dv_{dc}}{dt} + i_l \tag{2-14}$$

Since the system is assumed to be balanced,

$$\begin{cases} e_a + e_b + e_c = 0 \\ i_a + i_b + i_c = 0 \end{cases} \tag{2-15}$$

Adding both sides of the three equations in (2-13) and using (2-15), one can write

$$v_{Nn} = -\frac{v_{an} + v_{bn} + v_{cn}}{3} \tag{2-16}$$

Therefore, v_{an}, v_{bn} and v_{cn} could be derived as

$$\begin{cases} v_{an} = v_{aN} - \dfrac{v_{an} + v_{bn} + v_{cn}}{3} \\ v_{bn} = v_{bN} - \dfrac{v_{an} + v_{bn} + v_{cn}}{3} \\ v_{cn} = v_{cN} - \dfrac{v_{an} + v_{bn} + v_{cn}}{3} \end{cases} \tag{2-17}$$

Using a dc component and a fundamental m component to replace the switch function with its low-frequency component (following concept of average modeling), it could be shown as

$$\begin{cases} S_a = \dfrac{1}{2} + \dfrac{1}{2} m_a \\ S_b = \dfrac{1}{2} + \dfrac{1}{2} m_b \\ S_c = \dfrac{1}{2} + \dfrac{1}{2} m_c \end{cases} \tag{2-18}$$

where

m_a, m_b and m_c are the modulation signals used to control the VSC switches.

It should be noted that

$$m_a + m_b + m_c = 0 \tag{2-19}$$

By substituting (2-18) and (2-19) in (2-11) and (2-17), one gets

$$\begin{cases} v_{an} = (\frac{1}{2} + \frac{1}{2} m_a) v_{dc} - \frac{\frac{3}{2} + \frac{1}{2}(m_a + m_b + m_c)}{3} v_{dc} \\ \quad = \frac{1}{2} m_a v_{dc} \\ v_{bn} = (\frac{1}{2} + \frac{1}{2} m_b) v_{dc} - \frac{\frac{3}{2} + \frac{1}{2}(m_a + m_b + m_c)}{3} v_{dc} \\ \quad = \frac{1}{2} m_b v_{dc} \\ v_{cn} = (\frac{1}{2} + \frac{1}{2} m_c) v_{dc} - \frac{\frac{3}{2} + \frac{1}{2}(m_a + m_b + m_c)}{3} v_{dc} \\ \quad = \frac{1}{2} m_c v_{dc} \end{cases} \tag{2-20}$$

By substituting (2-20) in (2-13), it can be deducted that

$$\begin{cases} e_a = R i_a + L \frac{di_a}{dt} + \frac{1}{2} m_a v_{dc} \\ e_b = R i_b + L \frac{di_b}{dt} + \frac{1}{2} m_b v_{dc} \\ e_c = R i_c + L \frac{di_c}{dt} + \frac{1}{2} m_c v_{dc} \end{cases} \tag{2-21}$$

By substituting (2-19) and (2-20) in (2-12), one can get

$$i_{dc} = \frac{1}{2}(m_a \cdot i_a + m_b \cdot i_b + m_c \cdot i_c) \tag{2-22}$$

By combining (2-14) and (2-22), the current equation for VSC can be rewritten as

$$\frac{1}{2}(m_a \cdot i_a + m_b \cdot i_b + m_c \cdot i_c) = C \frac{dv_{dc}}{dt} + i_l \tag{2-23}$$

Therefore, the differential equations for VSC become

$$\begin{cases} L\dfrac{di_a}{dt} = -Ri_a - \dfrac{1}{2}m_a v_{dc} + e_a \\ L\dfrac{di_b}{dt} = -Ri_b - \dfrac{1}{2}m_b v_{dc} + e_b \\ L\dfrac{di_c}{dt} = -Ri_c - \dfrac{1}{2}m_c v_{dc} + e_c \\ \dfrac{dv_{dc}}{dt} = -\dfrac{1}{C}i_l + \dfrac{1}{2C}(m_a \cdot i_a + m_b \cdot i_b + m_c \cdot i_c) \end{cases} \quad (2\text{-}24)$$

2.2.2 Small-Signal Linearization of the System

In order to decrease variables in (2-24), the ac source voltage in each phase can be represented as

$$\begin{cases} e_a = E_m \cos(\omega t) \\ e_b = E_m \cos(\omega t - 120^\circ) \\ e_c = E_m \cos(\omega t + 120^\circ) \end{cases} \quad (2\text{-}25)$$

where

E_m is the peak value of the ac source voltage in volts

ω is the angular frequency in radians per seconds ($\omega = 2\pi f$, $f = 60Hz$)

t is time in seconds

The current in each phase could be written as

$$\begin{cases} i_a = I_m \cos(\omega t + \phi) \\ i_b = I_m \cos(\omega t + \phi - 120^\circ) \\ i_c = I_m \cos(\omega t + \phi + 120^\circ) \end{cases} \quad (2\text{-}26)$$

where

I_m is the peak value of current in each phase in amperes

ϕ is the phase-shift between voltage and current in each phase in degrees

The modulation signal corresponding to each phase can be written as

$$\begin{cases} m_a = M\cos(\omega t + \theta) \\ m_b = M\cos(\omega t + \theta - 120^\circ) \\ m_c = M\cos(\omega t + \theta + 120^\circ) \end{cases} \tag{2-27}$$

where

M is the peak value of the modulation signal, which is also the modulation index if the peak value of the triangular signal is equal to 1

θ is the modulation angle in degrees

Substituting (2-25), (2-26) and (2-27) into (2-24), the differential equations for the VSC in abc frame can be presented as

$$\begin{cases} \dfrac{dI_m}{dt} = -\dfrac{Mv_{dc}}{2L}\cos(\theta-\phi) + \dfrac{E_m}{L}\cos\phi - \dfrac{R}{L}I_m \\ \dfrac{d\phi}{dt} = -\dfrac{Mv_{dc}}{2LI_m}\sin(\theta-\phi) - \dfrac{E_m}{LI_m}\sin\phi - \omega \\ \dfrac{dv_{dc}}{dt} = -\dfrac{3MI_m}{4C}\cos(\theta-\phi) - \dfrac{i_l}{C} \end{cases} \tag{2-28}$$

For the system, the inputs are M and θ; the outputs are v_{dc}, I_m and ϕ; the states variables are v_{dc}, I_m and ϕ. The general form of the system of equation (2-28) can be presented as

$$\begin{cases} \dfrac{d\underline{x}}{dt} = \underline{f}(\underline{x},\underline{u}) \\ \underline{y} = \underline{g}(\underline{x},\underline{u}) \end{cases} \tag{2-29}$$

where

$$\underline{x} = \begin{bmatrix} I_m \\ \phi \\ v_{dc} \end{bmatrix} \tag{2-30}$$

$$\underline{u} = \begin{bmatrix} M \\ \theta \end{bmatrix} \tag{2-31}$$

Equation (2-28) shows that VSC is a non-linear system. Hence, small-signal analysis is used to linearize the system equations around a steady-state operating point. The perturbed system is represented as

$$\frac{d}{dt}\Delta\underline{x} = \left.\frac{\partial \underline{f}}{\partial \underline{x}}\right|_{*} \Delta\underline{x} + \left.\frac{\partial \underline{f}}{\partial \underline{u}}\right|_{*} \Delta\underline{u} \tag{2-32}$$

where

$\left.\frac{\partial \underline{f}}{\partial \underline{x}}\right|_{*}$ and $\left.\frac{\partial \underline{f}}{\partial \underline{u}}\right|_{*}$ are the Jacobean matrices evaluated at the steady-state operating point and are given as

$$\left.\frac{\partial \underline{f}}{\partial \underline{x}}\right| = \begin{bmatrix} \frac{\partial f_1}{\partial I_m} & \frac{\partial f_1}{\partial \phi} & \frac{\partial f_1}{\partial v_{dc}} \\ \frac{\partial f_2}{\partial I_m} & \frac{\partial f_2}{\partial \phi} & \frac{\partial f_2}{\partial v_{dc}} \\ \frac{\partial f_3}{\partial I_m} & \frac{\partial f_3}{\partial \phi} & \frac{\partial f_3}{\partial v_{dc}} \end{bmatrix} \tag{2-33}$$

$$\left.\frac{\partial \underline{f}}{\partial \underline{u}}\right| = \begin{bmatrix} \frac{\partial f_1}{\partial M} & \frac{\partial f_1}{\partial \theta} \\ \frac{\partial f_2}{\partial M} & \frac{\partial f_2}{\partial \theta} \\ \frac{\partial f_3}{\partial M} & \frac{\partial f_3}{\partial \theta} \end{bmatrix} \tag{2-34}$$

The general form of the linearized system is

$$\begin{cases} \dfrac{d\underline{x}}{dt} = \underline{A}\underline{x} + \underline{B}\underline{u} \\ \underline{y} = \underline{C}\underline{x} + \underline{D}\underline{u} \end{cases} \tag{2-35}$$

where

A and B are given by (2-33) and (2-34), respectively;

$C = \begin{bmatrix} 0 & 0 & 1 \\ 0 & 1 & 0 \\ 1 & 0 & 0 \end{bmatrix}$; and

$D = \begin{bmatrix} 0 & 0 & 0 \\ 0 & 0 & 0 \\ 0 & 0 & 0 \end{bmatrix}$

The transfer function of the linearized system can be obtained by

$$H(s) = C(sI - A)^{-1}B + D \tag{2-36}$$

where I is the identity matrix.

The above transfer function is coded in Matlab (Appendix A), and can be used in judging the stability of the system.

2.2.3 Modeling of VSC in DQ Frame

In order to decrease the control complexity of the 3-phase circuit, Park's transformation is used to convert the 3-phase quantities from abc frame to synchronously-rotating direct–quadrature–zero (dq0) frame. At steady-state, the sinusoidal quantities will be represented by constant quantities in dq0 frame. Since only a 3-phase balanced system is studied in this work, the value associated with 0 axis will be zero.

The Park's transformation operator is defined as

$$P = \frac{2}{3}\begin{bmatrix} \cos(\omega t+\alpha) & \cos(\omega t-2\pi/3+\alpha) & \cos(\omega t+2\pi/3+\alpha) \\ \sin(\omega t+\alpha) & \sin(\omega t-2\pi/3+\alpha) & \sin(\omega t+2\pi/3+\alpha) \\ 0.5 & 0.5 & 0.5 \end{bmatrix} \tag{2-37}$$

where

ω is the angular frequency of the system and

α is the transformation angle.

Accordingly, the inverse transformation operator is defined as

$$P^{-1} = \begin{bmatrix} \cos(\omega t+\alpha) & -\sin(\omega t+\alpha) & 1 \\ \cos(\omega t-2\pi/3+\alpha) & -\sin(\omega t-2\pi/3+\alpha) & 1 \\ \cos(\omega t+2\pi/3+\alpha) & -\sin(\omega t+2\pi/3+\alpha) & 1 \end{bmatrix} \tag{2-38}$$

To transform 3-phase voltages to dq0 frame, the following operation is performed.

$$e_{dq0} = P \cdot e_{abc} \tag{2-39}$$

where

$$e_{dq0} = \begin{bmatrix} e_d \\ e_q \\ e_0 \end{bmatrix} \tag{2-40}$$

Substituting (2-21) and (2-37) into (2-39), the voltage in dq0 frame can be given as

$$\begin{cases} e_d = E_m \cdot \cos\alpha \\ e_q = -E_m \cdot \sin\alpha \\ e_0 = 0 \end{cases} \tag{2-41}$$

To transform 3-phase currents to dq0 frame, the following operation is performed.

$$i_{dq0} = P \cdot i_{abc} \tag{2-42}$$

where

$$i_{dq0} = \begin{bmatrix} i_d \\ i_q \\ i_0 \end{bmatrix} \tag{2-43}$$

Substituting (2-26) and (2-37) into (2-42), the current in dq0 frame can be given as

$$\begin{cases} i_d = I_m \cdot \cos(\phi) \\ i_q = -I_m \cdot \sin(\phi) \\ i_0 = 0 \end{cases} \tag{2-44}$$

The first 3 lines of (2-24) can be written as

$$\frac{d}{dt} i_{abc} = -\frac{R}{L} i_{abc} - \frac{v_{dc}}{2L} m_{abc} + \frac{1}{L} e_{abc} \tag{2-45}$$

where

$$i_{abc} = \begin{bmatrix} i_a \\ i_b \\ i_c \end{bmatrix} \tag{2-46}$$

$$m_{abc} = \begin{bmatrix} m_a \\ m_b \\ m_c \end{bmatrix} \tag{2-47}$$

$$e_{abc} = \begin{bmatrix} e_a \\ e_b \\ e_c \end{bmatrix} \tag{2-48}$$

By implementing Park's transformation on (2-45), one gets

$$\frac{d}{dt} i_d = -\frac{R}{L} i_d - \frac{M v_{dc}}{2L} \cos\theta + \frac{1}{L} e_d + \omega i_q \tag{2-49}$$

$$\frac{d}{dt} i_q = -\frac{R}{L} i_q - \frac{M v_{dc}}{2L} \sin\theta + \frac{1}{L} e_d - \omega i_d \tag{2-50}$$

According to KCL, the current on dc side in Figure 2-4 can be written as

$$i_{dc} = i_l + i_C = i_l + C\frac{d}{dt}v_{dc} \tag{2-51}$$

where

i_C is the current through the parallel capacitor

i_l is the load current

i_{dc} is the dc terminal current of the VSC

v_{dc} is the dc terminal voltage of the VSC

Therefore, (2-24) can be written in dq frame as

$$\begin{cases} \frac{d}{dt}i_d = -\frac{R}{L}i_d - \frac{Mv_{dc}}{2L}\cos\theta + \frac{1}{L}e_d + \omega i_q \\ \frac{d}{dt}i_q = -\frac{R}{L}i_q - \frac{Mv_{dc}}{2L}\sin\theta + \frac{1}{L}e_d - \omega i_d \\ C\frac{d}{dt}v_{dc} = i_{dc} - i_l \end{cases} \tag{2-52}$$

2.2.4 The Decoupling of VSC in DQ Frame

The voltage and current can be represented in dq frame in vector notation as

$$\begin{cases} \vec{E} = e_d + je_q \\ \vec{I} = i_d + ji_q \end{cases} \tag{2-53}$$

The power transferred by VSC is [26]

$$S = \frac{3}{2}\vec{E}\,\vec{I}^{*} = P + jQ = \frac{3}{2}[(e_d i_d + e_q i_q) + j(e_q i_d - e_d i_q)] \tag{2-54}$$

where

S is the complex power

P is active power

Q is reactive power

e_q can be set to zero by a phase lock loop (PLL). The PLL realization will be shown in the next chapter 3.3.2. Therefore,

$$\begin{cases} e_d = E_m \\ e_q = 0 \\ e_0 = 0 \\ \alpha = 0^\circ \end{cases} \tag{2-55}$$

In order to get unity power factor on the ac-side, the reactive power should be equal to zero. Therefore, ϕ should be zero and i_q should be set to zero. Therefore, (2-44) can be represented as

$$\begin{cases} i_d = I_m \\ i_q = 0 \\ i_0 = 0 \end{cases} \tag{2-56}$$

Hence, (2-54) becomes

$$S = P = \frac{3}{2} e_d i_d = \frac{3}{2} E_m I_m \tag{2-57}$$

From the above equation, it can be concluded that the active power flow is controlled through control of d-axis component of current, as the d-axis voltage is constant and decided by the grid.

Chapter 3

Proposed Battery Simulator System

The proposed battery simulator consists of two parts. The battery model part generates the reference signal for the output voltage of simulator according to the load current, while the VSC part converts grid power to dc power with the terminal voltage following the reference voltage from the battery model for the given load current. In this chapter, the details of battery model will be discussed including the choice of battery model, the realization of the battery model by a circuit as well as a C block in PSim. The control strategy of VSC will be specified including the design of the control loops, the tuning theory for PI controllers and the realization of the VSC in PSim.

3.1 Battery Model Realization

In this section, the battery model is realized by PSim.

3.1.1 Choice of Battery Model

In the battery simulator system, the electrical-circuit model proposed by M. Chen and G. Rincon-Mora, which was discussed in section 2.1.3.1, is used as the battery cell model which generates voltage reference signal for the VSC at variable input current values. The reasons for choosing such model are as follows.

1. Although the accuracy of the model is not as high as electrochemical model, the precision (in mA and mV calibration) is absolutely sufficient for the motor-drive system.

2. The computation complexity for such model is acceptable when compared with electrochemical model.

3. Such model can truly present both steady state and transient responses which give a reliable reference for the VSC.

4. Such model can simulate different types of cells including lithium-ion, lead-acid, NiCd, NiMH, and polymer-lithium which offer the battery emulator good potential to be adjusted to different types of batteries.

3.1.2 The Calculation of SoC

Current integration method, also named as "coulomb counting", is used to obtain SoC by measuring the battery current and integrating it in time. The SoC equation can be written as

$$SOC = \frac{Q_0 - (\int I_{\text{load}} dt / N_{\text{p}}) / 3600}{Q_{\max}} \tag{3-1}$$

where

Q_0 is the initial Ah of the battery in coulomb

$Q_{\max}$ is the nominal Ah of the battery in coulomb

N_p is the number of parallel branches of the battery bank

I_{load} is the battery current in A

Note that when the battery current is leaving its terminals (discharge), current is assumed to be in positive direction.

In M. Chen and G. Rincon-Mora's model, the self-discharge effect is represented by a parallel self-discharge resistance. In the realization process, when calculating SoC, the effect of self-discharge is taken into account directly by adding a self-discharge current. The new equation for SoC is

$$SoC = \frac{Q_0 - (\int I_{\text{load}} dt / N_{\text{p}} + \int I_{sd} dt) / 3600}{Q_{\max}} \tag{3-2}$$

where

I_{sd} is the self-discharge current.

3.1.3 Circuit-Oriented Realization of Battery Model

Fig. 3-1 shows the realization of the battery model. For the generation of SoC in circuit-oriented realization, the calculation process is as follows.

a. Battery current is measured and divided by the number of parallel branches in order to have the current in each cell.

b. Cell current and self-discharge current are integrated and then added up. The unit of the resulting value is As.

c. The As value is divided by 3600 in order to be translated into Ah.

d. The value found in step c is subtracted from the initial Ah of the battery to get the present value of battery Ah.

e. The current Ah of battery is divided by the nominal battery capacity to produces SoC.

The open circuit voltage is realized by a voltage controlled voltage source (VCVS). The input of VCVS is set as equation (2-4) with the help of Math Function Block and Control-to-Power Interface Block in PSim. The gain of the component is the number of cells in series in the battery pack. For example, to emulate the performance of Tesla Roadster's battery pack, which has 99 cells in series in each branch [3][27], the gain is set as 99.

Equation (2-5)-(2-9) are used as the input functions for the Math Function Block and Control-to-Power Interface Block to realize the steady state series resistance, short-term and long-term transient resistances as well as short-term and long-term transient capacitances. For each cell, since there is no variable capacitor component in PSim, the long-term transient capacitance is created by a fixed capacitance, in which the value is 4475 F, in parallel with a voltage-controlled current source (VCCS) which has the exponential part of equation (2-9) as the input for the gain. The same method is applied to realize short-term transient capacitance. A current controlled current source (CCCS), in which the gain is set to 1, is used to generate the terminal current of the battery model. The control signal of the CCCS is the load current going through the battery.

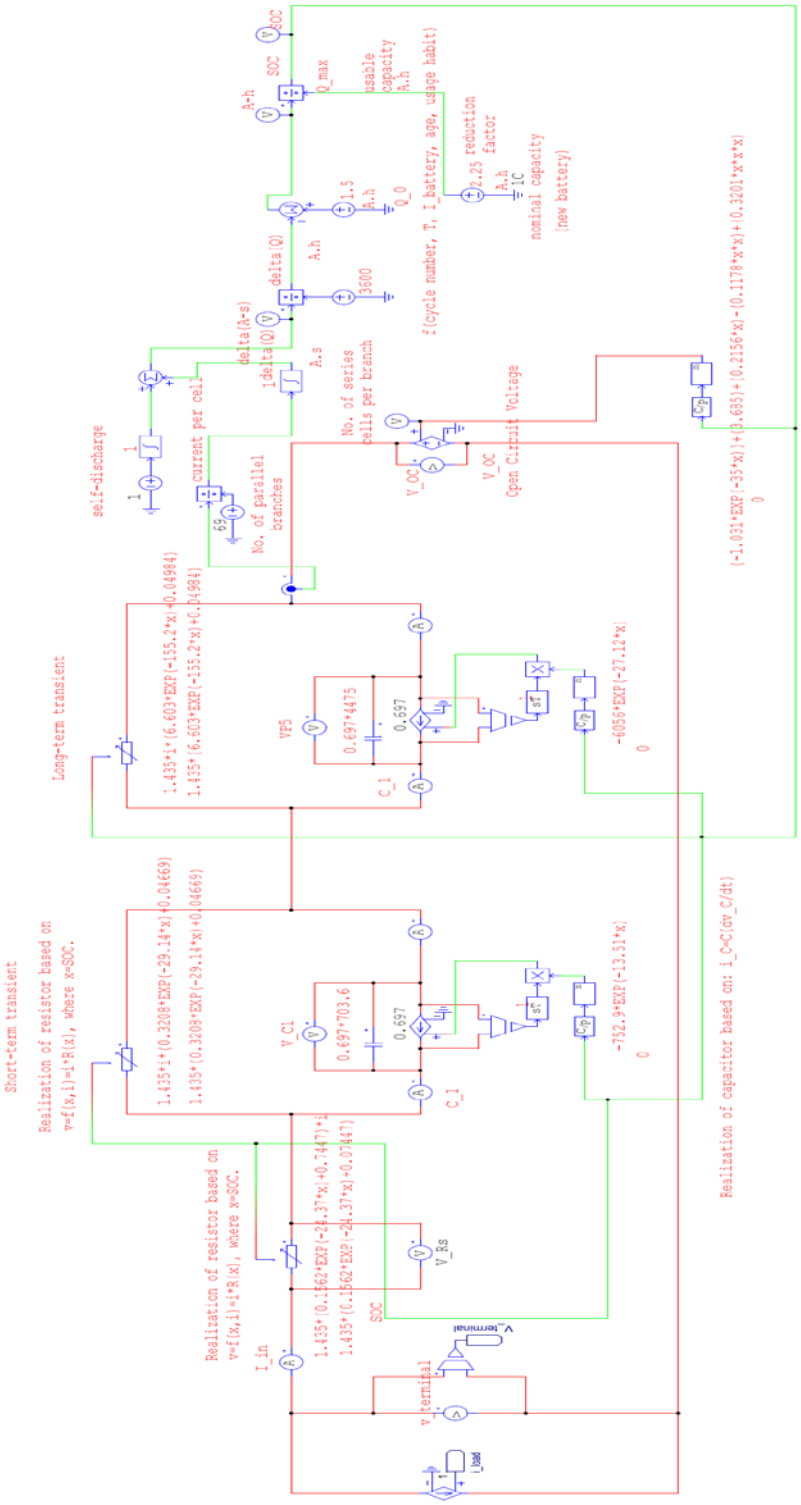

Figure 3-1 circuit-Oriented Realization of Battery Model

3.1.4 Equation-Based Realization of Battery Model

The realization for the battery model in section 3.1.3 gives a satisfying output characteristic which will be shown in the next chapter. However, this approach is appropriate for simulation purposes, while in practice where actual circuit components are integrated to make the battery simulator, realizing the battery model using mathematical equations is the proper approach. Therefore, a C block (a block with a code developed using C language) in PSim is used to reproduce the circuit that represented the model in the previous subsection. This block represents a micro-controller programmed based on the model equations.

3.1.4.1 Algorithm for the C Block

At time t, the battery model can be represented as follows.

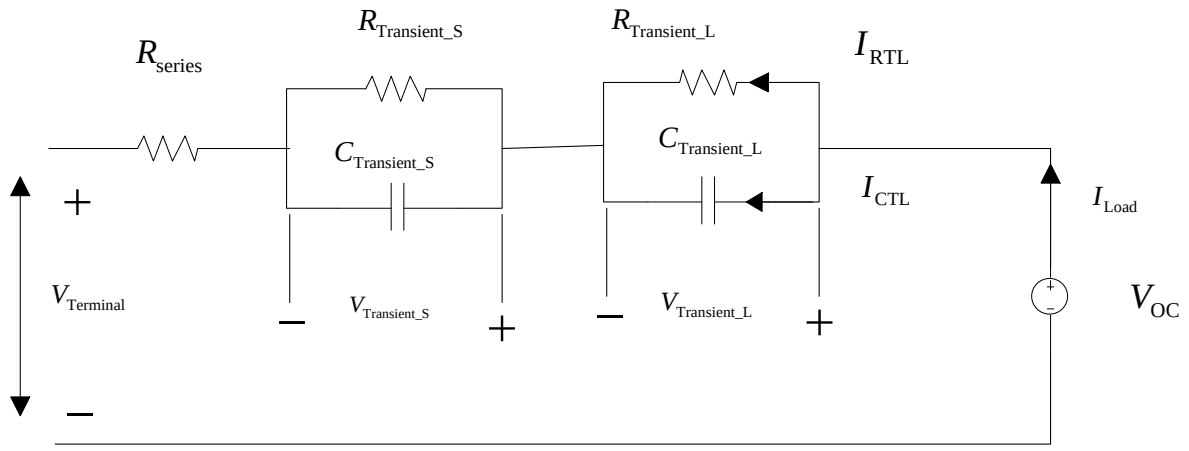

Figure 3-2 General Circuit for Battery Model

According to KVL and KCL,

$$(I_{\text{Load}} - I_{\text{CTL}}) \cdot R_{\text{Transient\_L}} = V_{\text{Transient\_L}} \tag{3-3}$$

$$C_{\text{Transient\_L}} \cdot \frac{dV_{\text{Transient\_L}}}{dt} = I_{\text{CTL}} \tag{3-4}$$

$$V_{\text{Terminal}} = V_{\text{OC}} - (V_{\text{Transient\_L}} + V_{\text{Transient\_S}} + I_{\text{Load}} \cdot R_{\text{series}}) \tag{3-5}$$

Combine (3-3) and (3-4), the long-term transient voltage could be solved for as

$$V_{\text{Transient\_L}} = (I_{\text{Load}} - C_{\text{Transient\_L}} \cdot \frac{dV_{\text{Transient\_L}}}{dt}) \cdot R_{\text{Transient\_L}} \tag{3-6}$$

Since PSim calculates in time steps, equation (3-6) can be rewritten as

$$V_{\text{Transient\_L}}[n] = (I_{\text{Load}} - C_{\text{Transient\_L}} \cdot \frac{V_{\text{Transient\_L}}[n] - V_{\text{Transient\_L}}[n-1]}{delt}) \cdot R_{\text{Transient\_L}} \tag{3-7}$$

where

$V_{\text{Transient\_L}}[n]$ is the $V_{\text{Transient\_L}}$ value at time step n,

$V_{\text{Transient\_L}}[n-1]$ is the $V_{\text{Transient\_L}}$ value at time step $n-1$, and

$delt$ is the time step.

In equation (3-7), rearranging terms results in

$$V_{\text{Transient\_L}}[n] = \frac{R_{\text{Transient\_L}} \cdot I_{\text{Load}} + \frac{C_{\text{Transient\_L}} \cdot R_{\text{Transient\_L}}}{delt} \cdot V_{\text{Transient\_L}}[n-1]}{1 + \frac{C_{\text{Transient\_L}} \cdot R_{\text{Transient\_L}}}{delt}} \tag{3-8}$$

Similarly, the short term transient voltage could be calculated as

$$V_{\text{Transient\_S}}[n] = \frac{R_{\text{Transient\_S}} \cdot I_{\text{Load}} + \frac{C_{\text{Transient\_S}} \cdot R_{\text{Transient\_S}}}{delt} \cdot V_{\text{Transient\_S}}[n-1]}{1 + \frac{C_{\text{Transient\_S}} \cdot R_{\text{Transient\_S}}}{delt}} \tag{3-9}$$

By substituting (3-8) and (3-9) into (3-5), the terminal voltage of the battery can be determined.

3.1.4.2 Creation of C Block in PSim

In PSim, the C block is created with 6 inputs and 5 outputs (see Figure 3-3). The 6 inputs, from top to bottom, are the initial Ah of the battery, the nominal capacity of the battery, the number of cells in series per branch, the total number of branches in the pack, the load current and the self-discharge current. The 5 outputs, from top to bottom, are the value of SoC, the terminal voltage, the short-term transient network voltage, the long-term transient network voltage and the open circuit voltage. The code for C block is given in Appendix B.

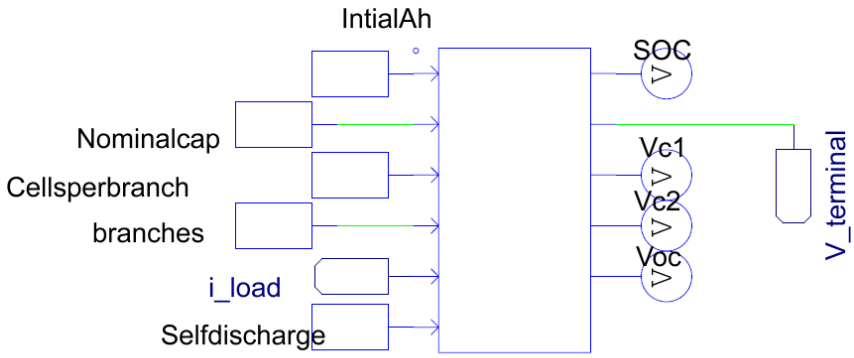

Figure 3-3 Realization of Battery Model by a C Block

By changing the input values for number of cells per branch and total number of branches, different types of battery pack structures can be created. It should be noted that if the number of cells in series is n and number of branches is m, all per-cell resistance values will be multiplied by $\frac{n}{m}$, while all per-cell capacitance values will be multiplied by $\frac{m}{n}$.

3.2 The Control Strategy for VSC

As mentioned in section 2.2.4, according to the decoupling method in dq frame, the d-axis current component is controlled in order to control the power flow of VSC. Therefore, a cascade control scheme is applied to control the dc-side output voltage of the VSC according to the reference signal provided by the battery model. The dc-side current (i.e., the battery terminal current) is constructed based on the load current profile. The control loop is composed of two loops which are the inner current loop and the outer voltage loop. The outer loop produces the reference signal for the inner loop.

3.2.1 The Creation of Inner Current Loop Control

As previously explained, i_q will be set to zero to achieve the unity power factor, while (2-49) is used to create the inner current loop to follow the load current on the dc side. By applying Laplace transform to (2-49), one gets

(3-10)

$$\frac{Mv_{dc}}{2}\cos\theta = -(sL+R)i_d + \omega L i_q + e_d$$

In (3-10), i_d is the output of the inner current loop. $\omega L i_q$ can be removed by a feedfoward loop [30] but due to its minor effect, it is ignored in this work. In order to have the current follow the reference, a proportional-integral (PI) controller is used. The block diagram of the inner current control loop is shown in Figure 3-4.

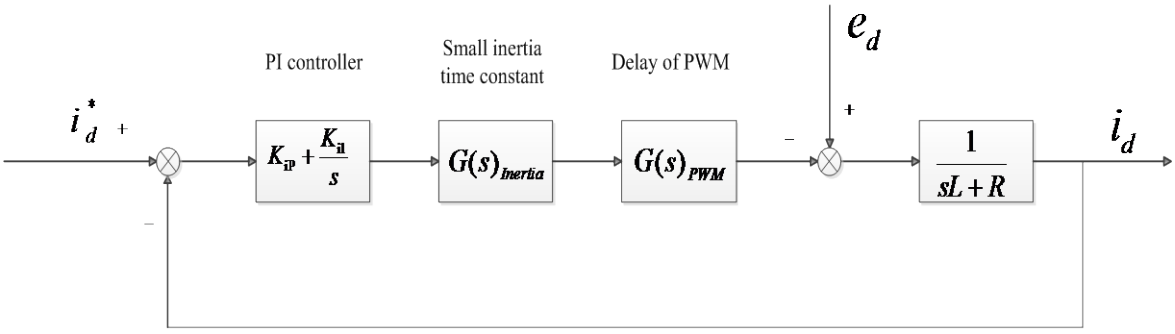

Figure 3-4 Inner Current Control Loop

The transfer function of PI controller in s domain can be written as

$$G(s)_{PI\ Inner} = K_{iP} + \frac{K_{iI}}{s} \tag{3-11}$$

where

K_{iP} is the proportional gain of PI controller, and

K_{iI} is the integral gain of PI controller.

The small-inertia time constant for VSC is represented in the following transfer function [31]

$$G(s)_{Inertia} = \frac{1}{1+sT} \tag{3-12}$$

where

T is the inverse of the PWM switching frequency.

The delay of PWM could be represented as [29]

$$G(s)_{PWM} = \frac{K_{PWM}}{1+0.5Ts} \tag{3-13}$$

where

T is the inverse of the PWM switching frequency, and

K_{PWM} is the equivalent gain of PWM which is defined as

$$K_{PWM} = \frac{\text{Peak value of AC voltage}}{\text{Peak value of carrier wave}} \tag{3-14}$$

In order to simplify the block diagram, the small-inertia time constant block and the delay of PWM could be combined as [33]

$$G(s)_{PWM\ \&\ Time\ Inertia} = \frac{K_{PWM}}{1+1.5Ts} \tag{3-15}$$

Hence, the modified inner current control loop block diagram is as shown in Figure 3-5.

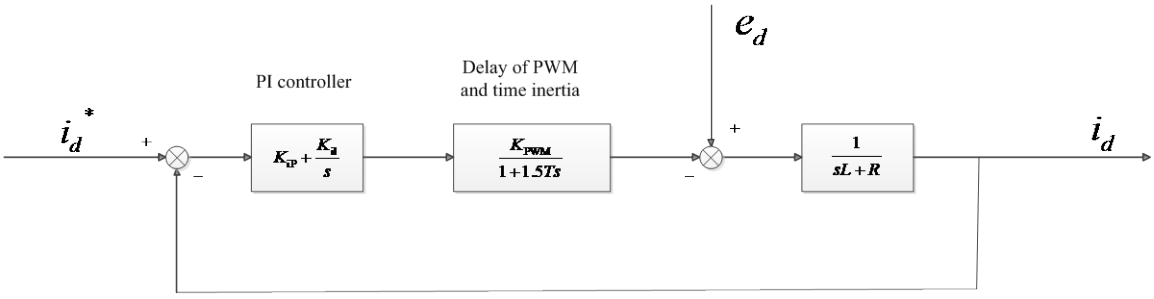

Figure 3-5 Simplified Inner Current Loop

The open-loop transfer function of the inner current loop can be given as

$$G(s)_{\mathrm{IOP}} = \frac{(sK_{\mathrm{ip}} + K_{\mathrm{iI}})K_{\mathrm{PWM}}}{s(1.5Ts+1)(sL+R)} \tag{3-16}$$

In the following subsections, two approaches for the design of the PI controller will be presented.

3.2.1.1 Type I Design

Let $K_{\mathrm{ip}} = \frac{L}{R}K_{\mathrm{iI}}$. Equation (3-16) can then be transformed to

$$G(s)_{\mathrm{IOP}} = \frac{K_{\mathrm{ip}}K_{\mathrm{PWM}}}{s(1.5Ts+1)} \tag{3-17}$$

From the above equation, it can be seen that the inner control loop has become a typical Type I system [32] which is also called a second-order system. The general form of the close-loop transfer function of Type I system is

$$G(s)_I = \frac{{\omega_n}^2}{s^2 + 2\xi\omega_n s + {\omega_n}^2} \tag{3-18}$$

where

ω_n is the natural frequency of the system in radian per second, and

ξ is the damping ratio.

Based on the explanations regarding Type I system in Appendix C, ξ is usually set to 0.707. Therefore, the parameters of the PI controller can be solved for as

$$\begin{cases} K_{\mathrm{ip}} = \dfrac{L}{3TK_{\mathrm{PWM}}} \\ K_{\mathrm{iI}} = \dfrac{R}{3TK_{\mathrm{PWM}}} \end{cases} \tag{3-19}$$

3.2.1.2 Type II Design

When $\omega_c L$ is far greater than R, in which ω_c is the cutoff frequency of the inner current loop, the influence of R can be ignored. Therefore, the open-loop transfer function of the inner current loop can be simplified as

$$G(s)_{\mathrm{IOP}} = \frac{(sK_{\mathrm{ip}} + K_{\mathrm{iI}})K_{\mathrm{PWM}}}{s(1.5Ts+1)(sL)} \tag{3-20}$$

The above equation shows that the inner current loop is a typical type II system [32], with the general form of

$$G(s)_{\mathrm{II}} = \frac{K(\tau^* s+1)}{s^2(T^* s+1)} \tag{3-21}$$

The bandwidth of the type-II system is defined as

$$h = \frac{\tau^*}{T^*} \tag{3-22}$$

$h = 5$ is usually applied to achieve a good trade-off between overshoot and settling time, according to the study of Type II system in appendix C. Therefore, parameters of the PI controller can be solved for as

$$\begin{cases} K_{\mathrm{ip}} = \dfrac{6L}{15TK_{\mathrm{PWM}}} \\ K_{\mathrm{iI}} = \dfrac{6L}{112.5T^2K_{\mathrm{PWM}}} \end{cases} \tag{3-23}$$

3.2.2 The Outer Voltage Control Loop

By applying Laplace transform to (2-51), one gets

$$v_{dc} = \frac{1}{sC}(I_{dc} - I_l) \tag{3-24}$$

The delay to the VSC by the PLL will be taken into consideration. In order to make the output voltage follow the reference voltage provided by the battery model, a PI controller is used. The signal after PI controller works as the reference signal for the inner current loop. Hence, a simplified inner

current loop is created. Since the inner loop is created by the ac side, a block to transfer the ac signal to dc signal should be implied. Therefore, the block diagram of the outer voltage loop is as shown in Figure 3-6.

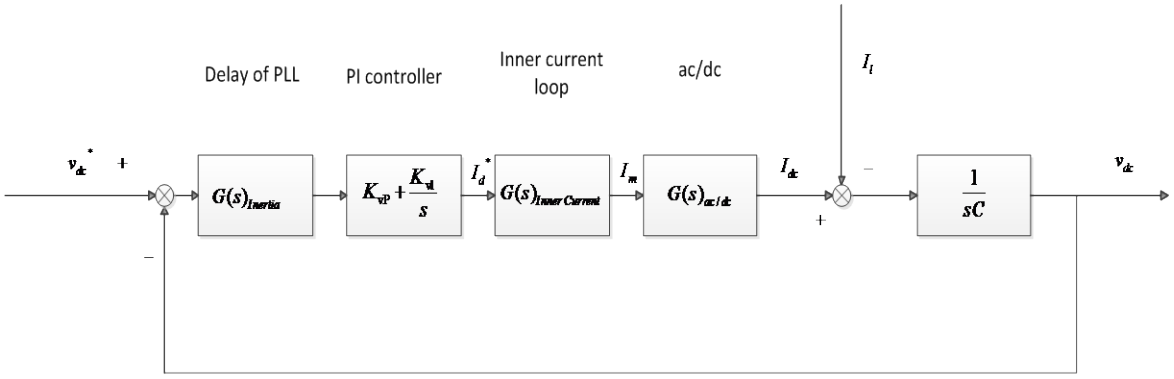

Figure 3-6 General Outer Voltage Loop

The transfer function of PI controller in s domain can be written as

$$G(s)_{PI\ Outer} = K_{vP} + \frac{K_{vI}}{s} \tag{3-25}$$

where

K_{vP} is the proportional gain of PI controller, and

K_{vI} is the integral gain of PI controller.

The delay of PLL can be written as [33]

$$G(s)_{Inertia} = \frac{1}{1+s\tau_{PLL}} \tag{3-26}$$

where

τ_{PLL} is the time constant representing the delay of PLL.

The inner current loop can be approximated as [29]

$$G(s)_{Inner\ Current} = \frac{I_d}{I_d^*} \approx \frac{1}{3Ts+1} \tag{3-27}$$

Equation (2-56) has proved that the current projection on d axis equals to the peak of the current on ac side. Therefore, (3-27) could be written as

$$G(s)_{Inner\ Current} = \frac{I_m}{I_d^*} \approx \frac{1}{3Ts+1} \tag{3-28}$$

By substituting (2-25) and (2-26) into (2-22), the relation between I_m and I_{dc} can be found as

$$G(s)_{ac/dc} = \frac{I_{dc}}{I_m} = 0.75M\cos\theta \tag{3-29}$$

Since the switching angle θ is a very small number and usually negligible, $\cos\theta$ can be approximated to 1. If the peak value of the triangular signal is equal to 1, the modulation index M varies from 0 to 1 according the load current. In this work, M is arbitrarily set to 1. Similar assumptions have also been made in [31] and [33]. Therefore, (3-29) is simplified as

$$G(s)_{ac/dc} = \frac{I_{dc}}{I_m} = 0.75 \tag{3-30}$$

The open-loop transfer function, in which the same simplification as in (3-15) has been implemented, becomes

$$G(s)_{\mathrm{VOP}} = \frac{0.75K_{\mathrm{vp}}\left(\frac{K_{\mathrm{vp}}}{K_{\mathrm{vI}}}s+1\right)}{C\frac{K_{\mathrm{vp}}}{K_{\mathrm{vI}}}s^2[1.5T(3T+\tau_{\mathrm{v}})s+1]} \tag{3-31}$$

The above equation indicates that the outer voltage loop is a typical type II system. So, the same design criterion as in type II design in inner current loop can be used directly. The parameters of the PI controller can be solved for as

$$\begin{cases} K_{\text{vp}} = \dfrac{4C}{5(\tau_v + 3T)} \\ K_{\text{vI}} = 5(\tau_v + 3T) \end{cases} \tag{3-32}$$

3.3 The Realization of VSC

3.3.1 The Circuit Realization of Park's Transformation

The calculation of Park's transformation and its inverse transformation are realized by 2 sub-circuits in PSim. The block shown in Figure 3-7 is used to present park's transformation.

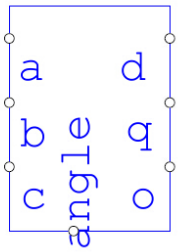

Figure 3-7 Park's Transformation Block

The circuit diagram for the above block is

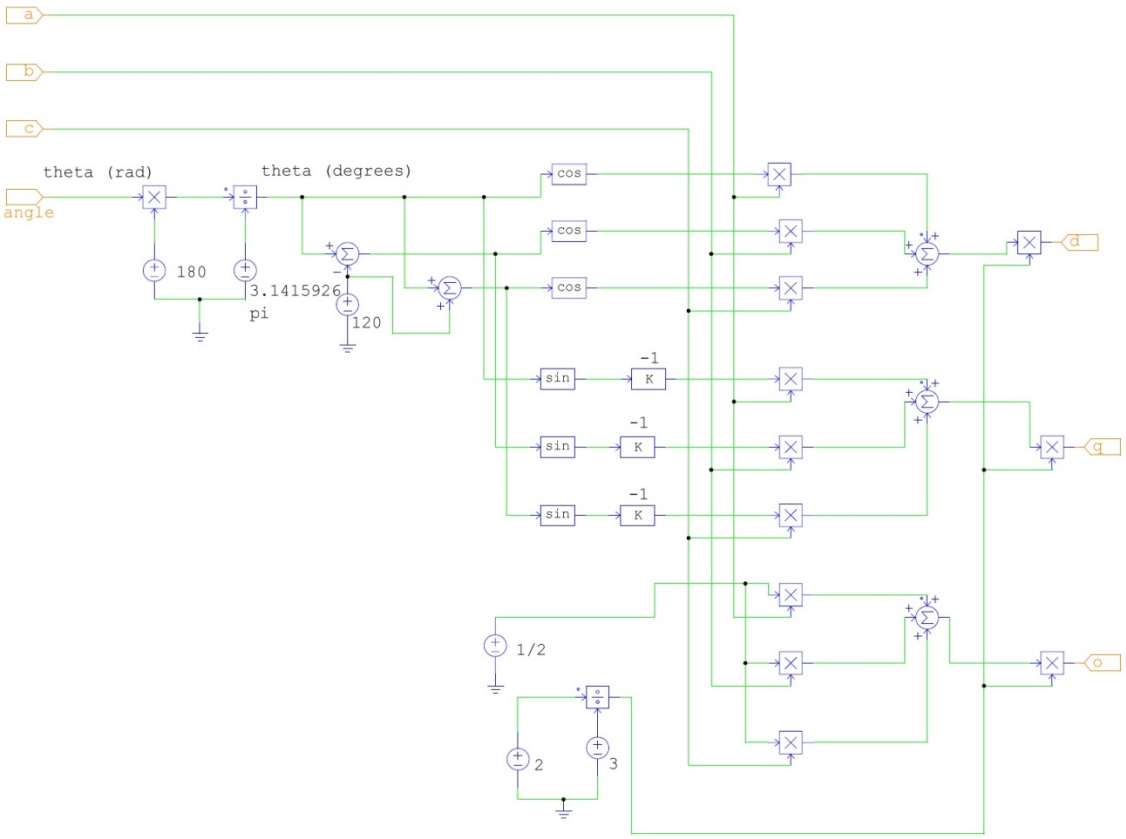

Figure 3-8 Circuit Diagram for Park's Transformation Block

The Inverse Park's transformation block is

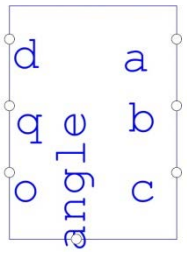

Figure 3-9 Inverse Park's Transformation Block

The circuit diagram for the above block is

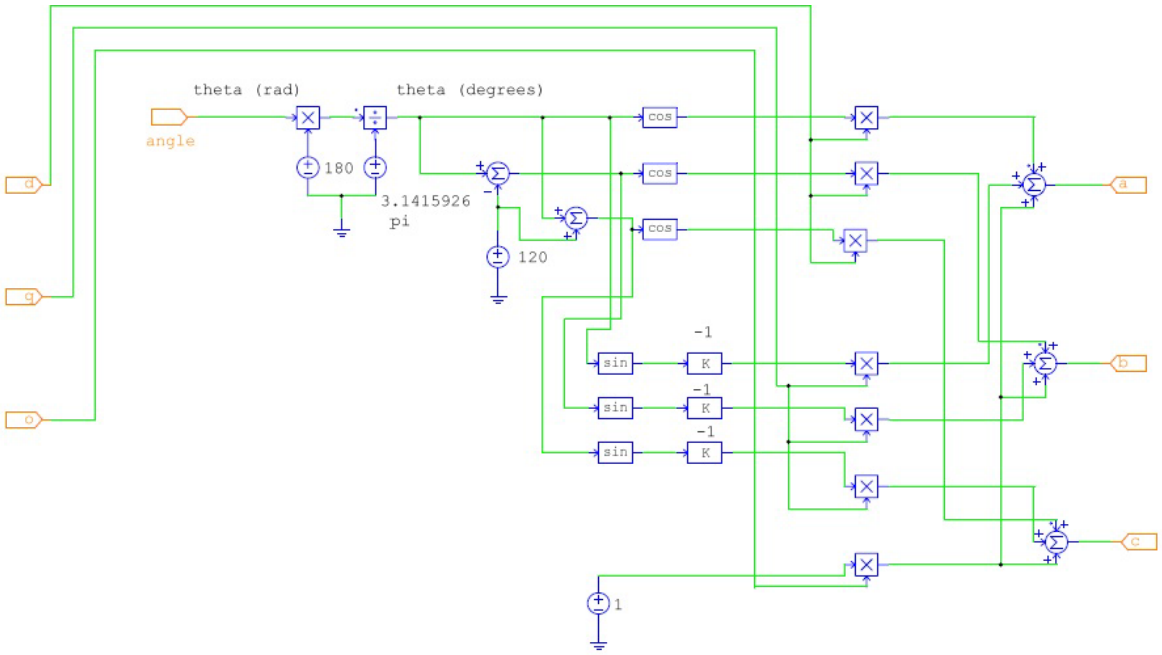

Figure 3-10 Circuit Diagram for Inverse Park's Transformation Block

3.3.2 The Realization of Phase Lock Loop (PLL)

A unit time delay is used to generate a time delay of one time step in the simulation in order to generate the transformation angle. The PLL is realized as

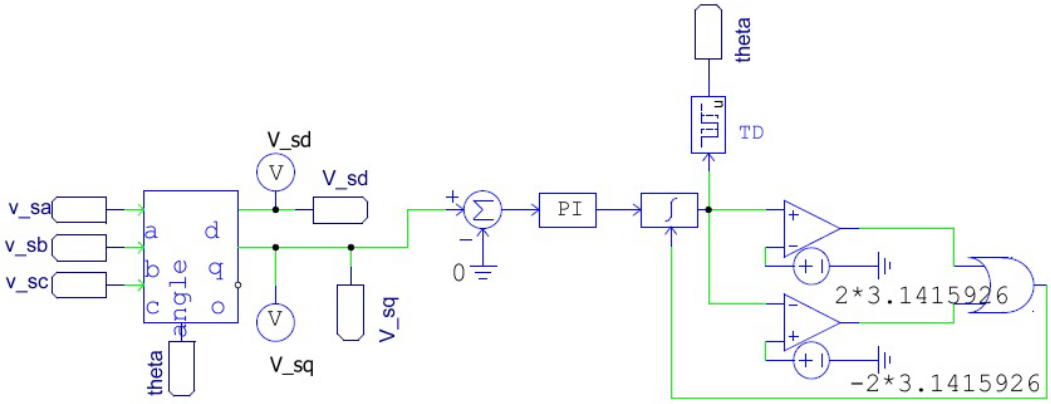

Figure 3-11 PLL

3.3.3 The Realization of VSC and its Controller

The VSC and its control circuit are realized by PSim as shown in Figure 3-12.

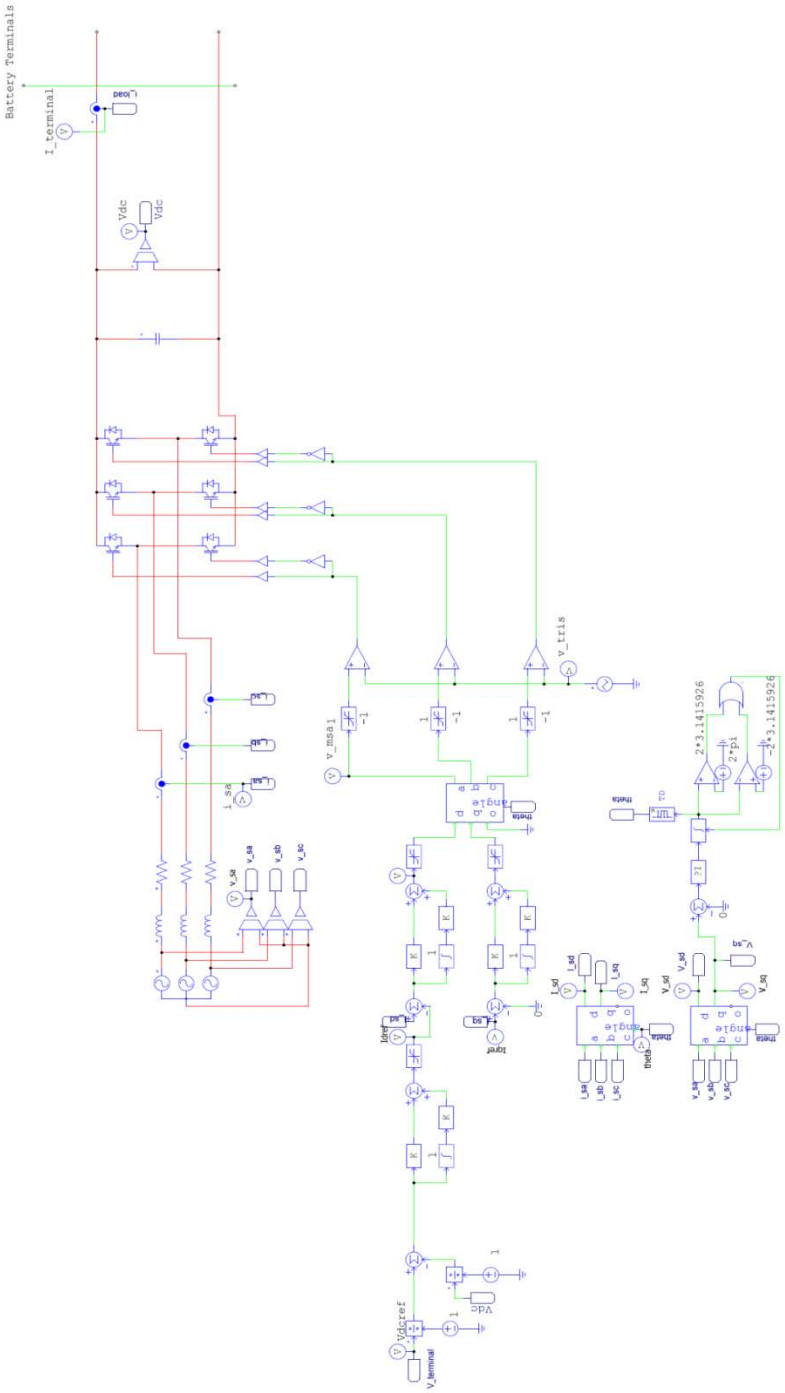

Figure 3-12 VSC and its Control Circuit

Chapter 4
Simulation Results and Analysis

In this chapter, simulation results, including simulation for different realizations of battery models and simulation for different loads under different tuning methods, will be presented.

4.1 Simulation of Battery Model

The realization of battery model by circuit was shown in Figure 3-1 and the realization of battery model by C block was shown in Figure 3-3. The load current (input to the model), which starts at 50 A, increases to 200 A and decreases to -200 A, in steps, as shown in Figure 4-1.

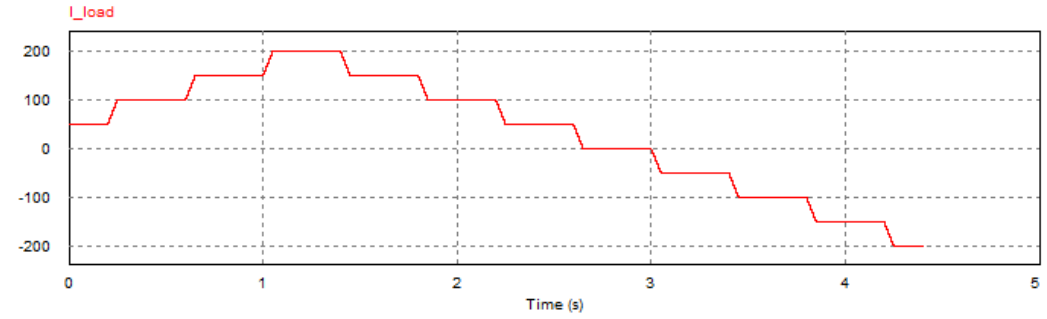

Figure 4-1 Load Current (input to the battery model)

The SoC patterns generated by the circuit and C block are shown in Figure 4-2 in red and blue colors, respectively.

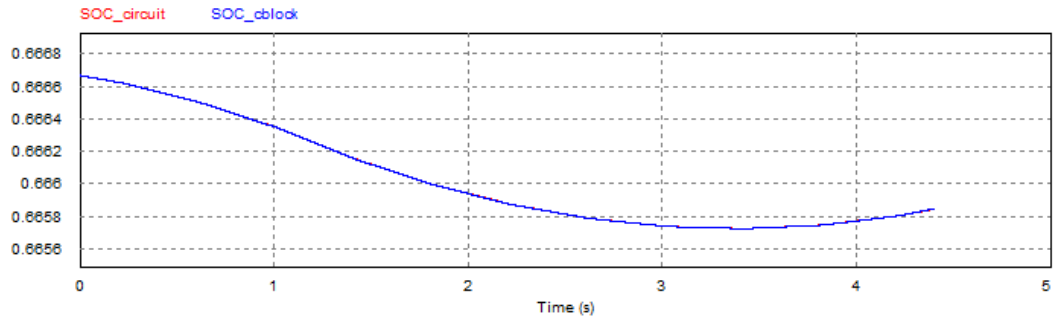

Figure 4-2 SoC

The terminal voltages generated by circuit model (red) and by C block (blue) are shown in Figure 4-3.

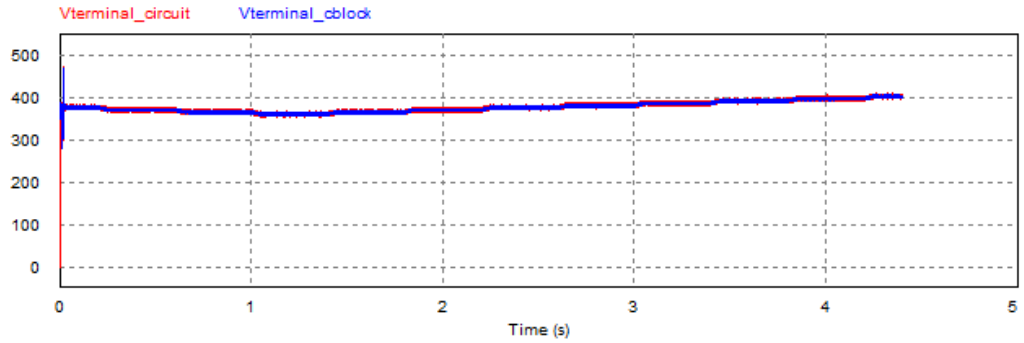

Figure 4-3 Terminal Voltage

The short-term transient network voltages generated by circuit model (red) and by C block (blue) are shown in Figure 4-4.

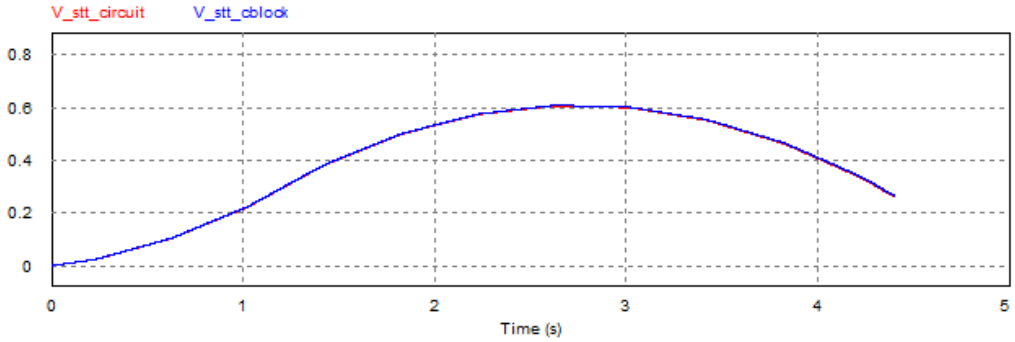

Figure 4-4 Short-term Transient Network Voltage

The long-term transient network voltages generated by circuit model (red) and by C block (blue) are shown in Figure 4-5.

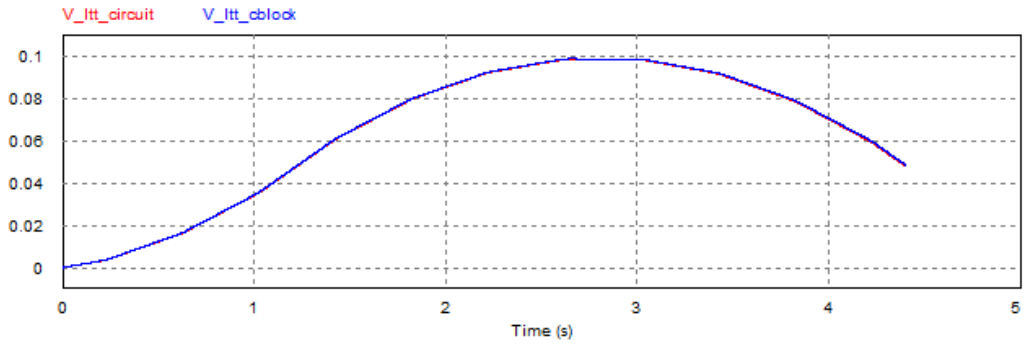

Figure 4-5 Long-term Transient Network Voltage

The open circuit voltages generated by circuit model (red) and by C block (blue) are show in Figure 4-6.

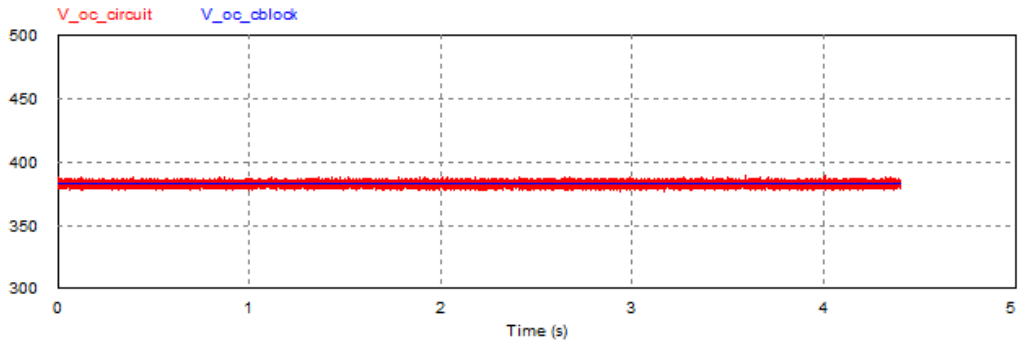

Figure 4-6 Open Circuit Voltage

From the above figures, it can be easily observed that the C block realization's curves overlap the circuit model realization's curves, but with less ripples, especially in the open circuit voltage. Generally, the terminal voltages produced by both methods, which works as the reference voltage for VSC, have sufficient accuracy and could be replaced by one another. Therefore, later simulations would be based on the C block realization for the battery model, since C block can be implemented easily in the lab using a microcontroller.

4.2 Simulation for Battery Simulator with Ideal Load

4.2.1 Creation of the Ideal Load

The ideal load, which requires power-related variable current, will be created by a dc/dc full bridge converter. A PI controller is used to adjust the error of feedback current and reference current, while PWM technique is also used to generate the switching signals.

The circuit diagram of the ideal load is shown in Figure 4-7.

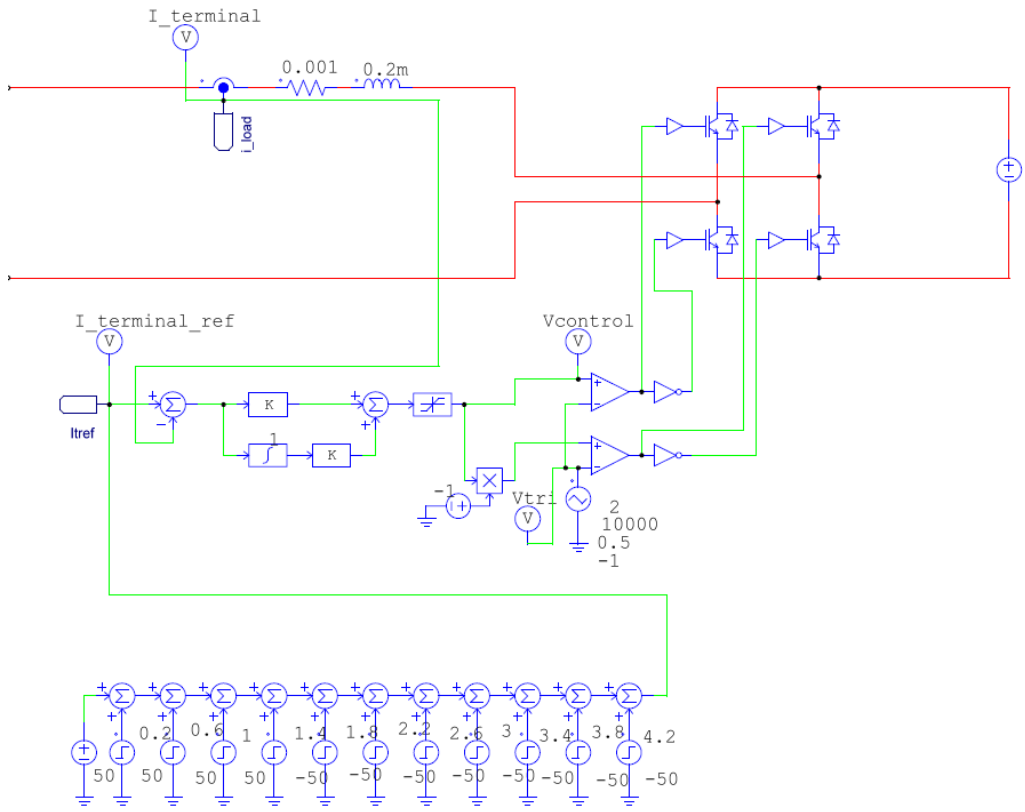

Figure 4-7 Ideal Load

The string of step voltage sources works to generate a variable reference signal for the load current. While the load current is a negative value, the load works as a power source and the battery emulator works in the charging mode. To change the step voltage value to target value could achieve the control of load current value.

Tuning of gains of the PI controller follows the practice of trials and errors. According to the simulation results, the system works well when the PI controller is adjusted to the same parameters of the PI controller used in the inner current loop. To simplify the system, the switching frequency for the carrier wave is also set as the same frequency of the carrier wave for the VSC system. It should be noted that the value for the dc power source on the right side of the IGBT should be adapted according to the required v_{dc} on the left side.

A resistor and an inductor are also used to help remove the ripples created by the PWM switching and facilitate control of current. Values for R and L depend on the unwanted harmonic frequency and could be decided by trials and error.

4.2.2 Integration of VSC and Ideal Load

The lithium battery pack used in the Tesla Roadster is utilized as the reference battery pack. Parameters for the battery circuit block are set as given in Table 4-1.

Table 4-1 C Block Parameters for Battery Model

Initial Ah	1.5
Nominal capacity	2.25
No. of Cells per branch	99
No. of Branches	69
Self-discharge current (A)	1

The parameters for the VSC are chosen as given by Table 4-2.

Table 4-2 VSC Parameters

AC Source line-line voltage (V)	100
Resistance per phase (Ω)	0.001
Inductance per phase (H)	0.0001
Capacitance on dc side (F)	0.0005

The parameters for PWM are given in Table 4-3.

Table 4-3 PWM Parameters

Switching frequency (Hz)	10000
Peak to peak voltage (V)	2
Offset voltage (V)	-1
Carrier waveform	Triangular
Duty cycle	0.5
Simulation time step	5E-6

The circuit diagram of the overall system is shown in Figure 4-8.

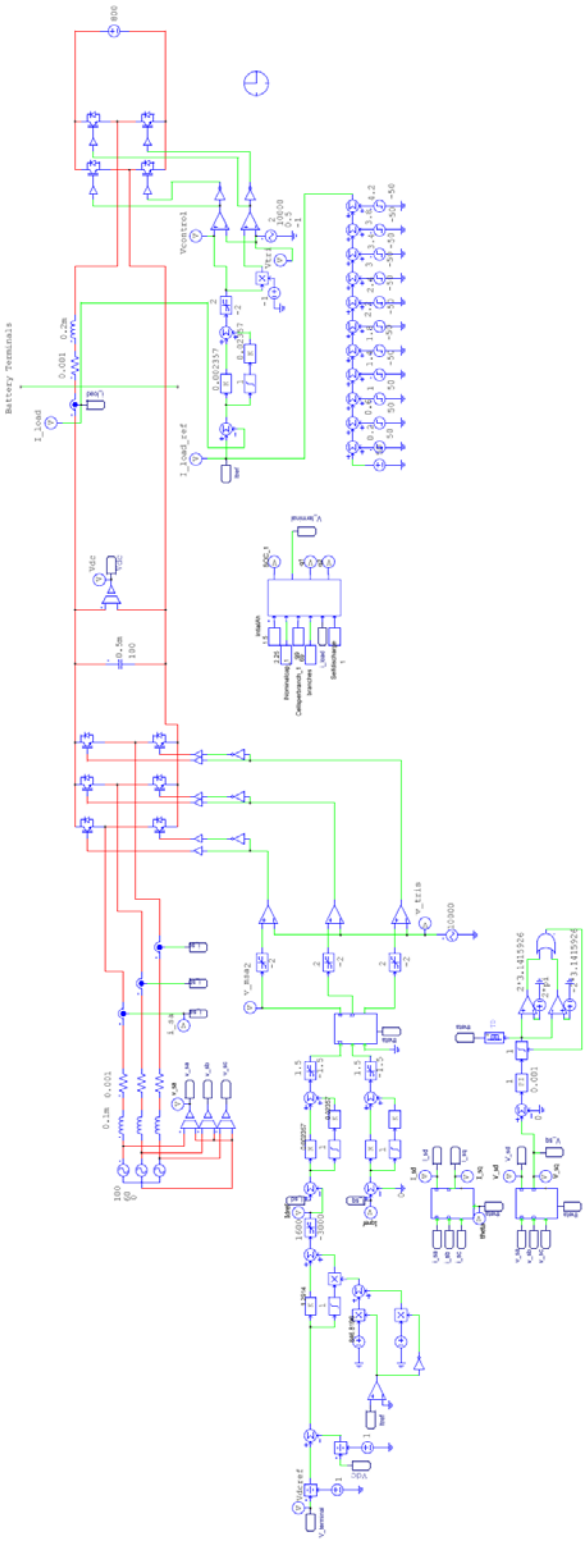

Figure 4-8 Battery Simulator-Ideal Load Integration

4.2.2.1 Type I Design

By substituting parameters from Table 4-2 and Table 4-3 into (3-19) and (3-32), parameters for PI controllers can be solved for as given in Table 4-4.

Table 4-4 Gains for PI Controllers under Type I Design

K_{ip}	0.002357
K_{iI}	0.02357
K_{vp}	1.2914
K_{iI}	846.8196

The simulation results are shown in Figure 4-9, Figure 4-10, Figure 4-11 and Figure 4-12. From Figure 4-9 it can be seen that the load current I_{load} successfully follows the reference load current $I_{load\ ref}$, starting from 50 A , peaking at 200 A , and finally decreasing to -200 A . The VSC output voltage V_{dc} successfully follows the reference voltage $V_{dc\ ref}$ generated by the battery model, which proves the effectiveness of tuned parameters for the PI controller used in the outer voltage loop. The SoC correctly decreases with the increase of load current, and increases when the load current becomes negative which proves the battery emulator is capable of working in both charging and discharging states. The current on d axis i_{sd} successfully follows the reference signal i_{dref} generated by the outer voltage loop, which proves the effectiveness of the tuned parameters for the PI controller used in the inner current loop.

From Figure 4-10 and Figure 4-11, it can be seen that the phase voltage v_{sa} is in phase with phase current i_{sa} in the discharging state while v_{sa} is 180 degree out of phase with i_{sa} in the charging state. The quality of the waveform for the phase current is good as no enormous distortion is observed.

From Figure 4-12, it can be seen that the system does not achieve steady state until 0.2 seconds and the maximum transient load current I_{load} is approximately 400 A while the maximum transient VSC output voltage V_{dc} is approximately 800 V.

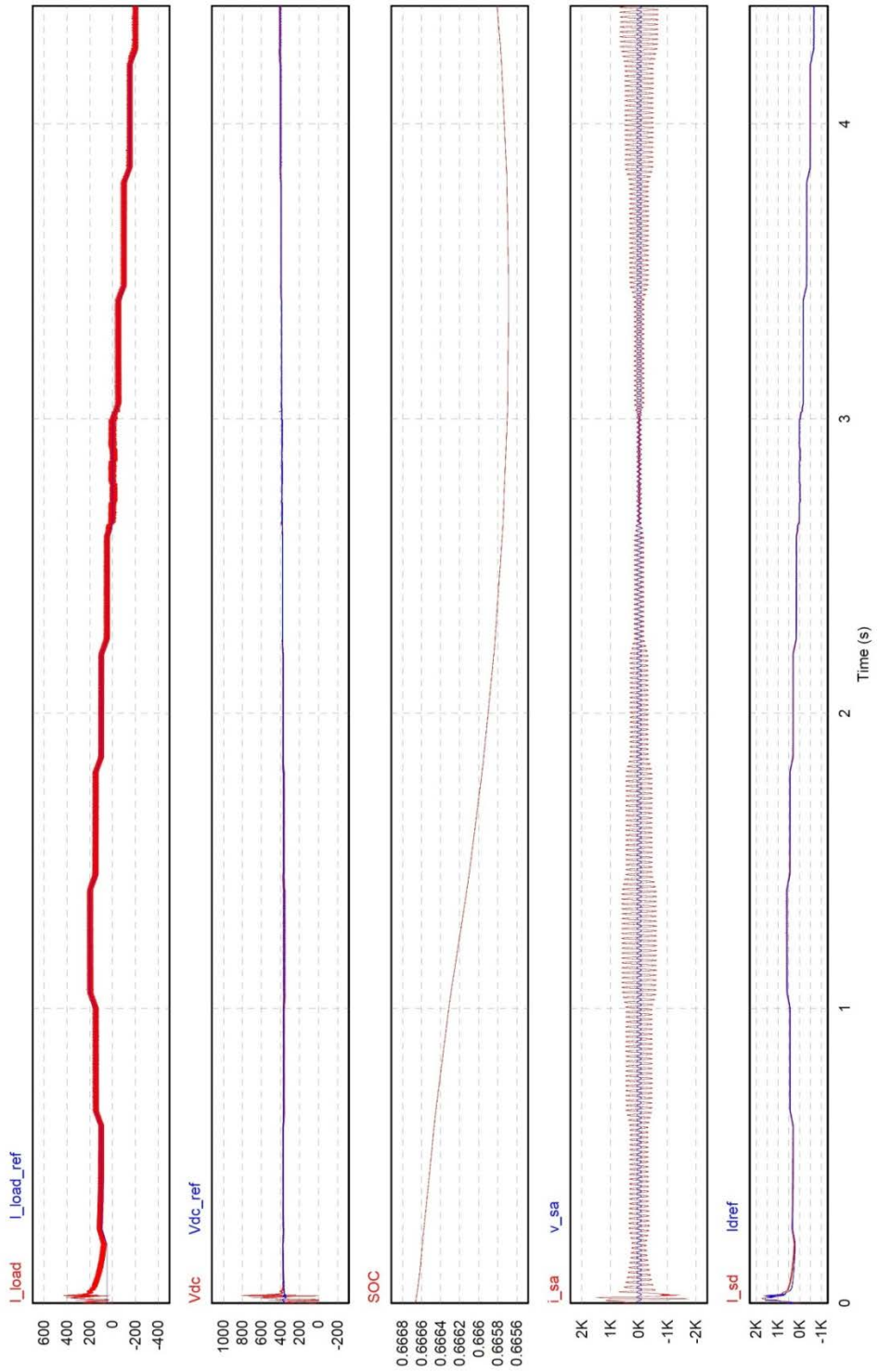

Figure 4-9 Simulation Results for VSC-Ideal Load Combination under Type I Design

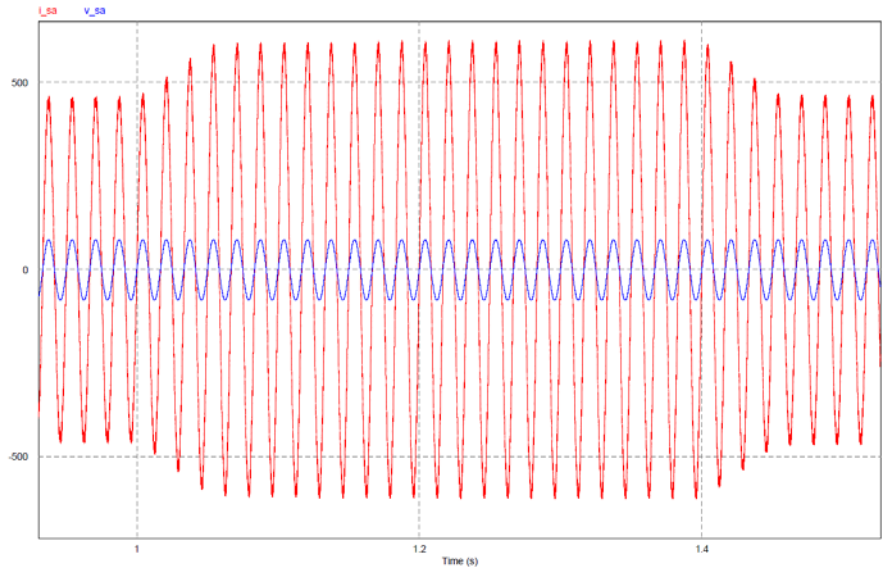

Figure 4-10 Zoomed-in Plot of Phase Voltage and Phase Current for Discharging State under Type I Design

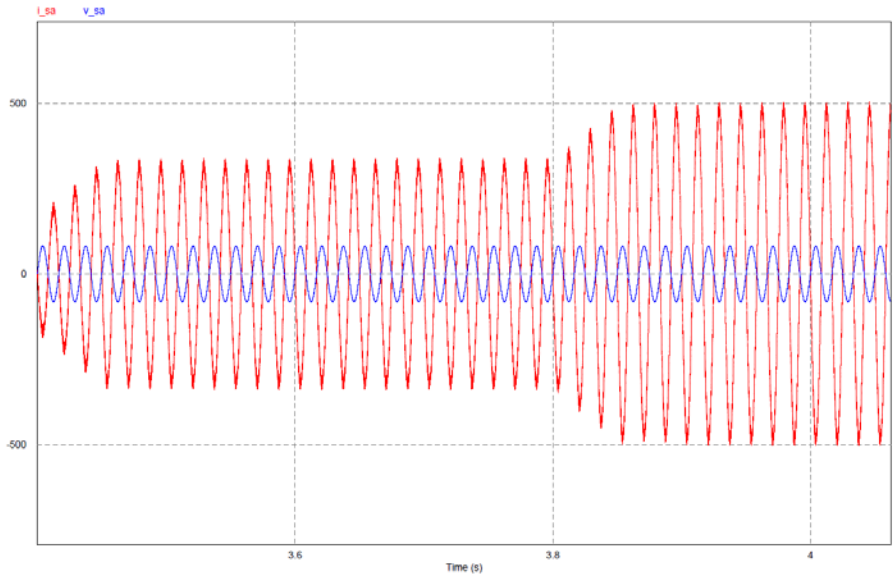

Figure 4-11 Zoomed-in Plot of Phase Voltage and Phase Current for Charging State under Type I Design

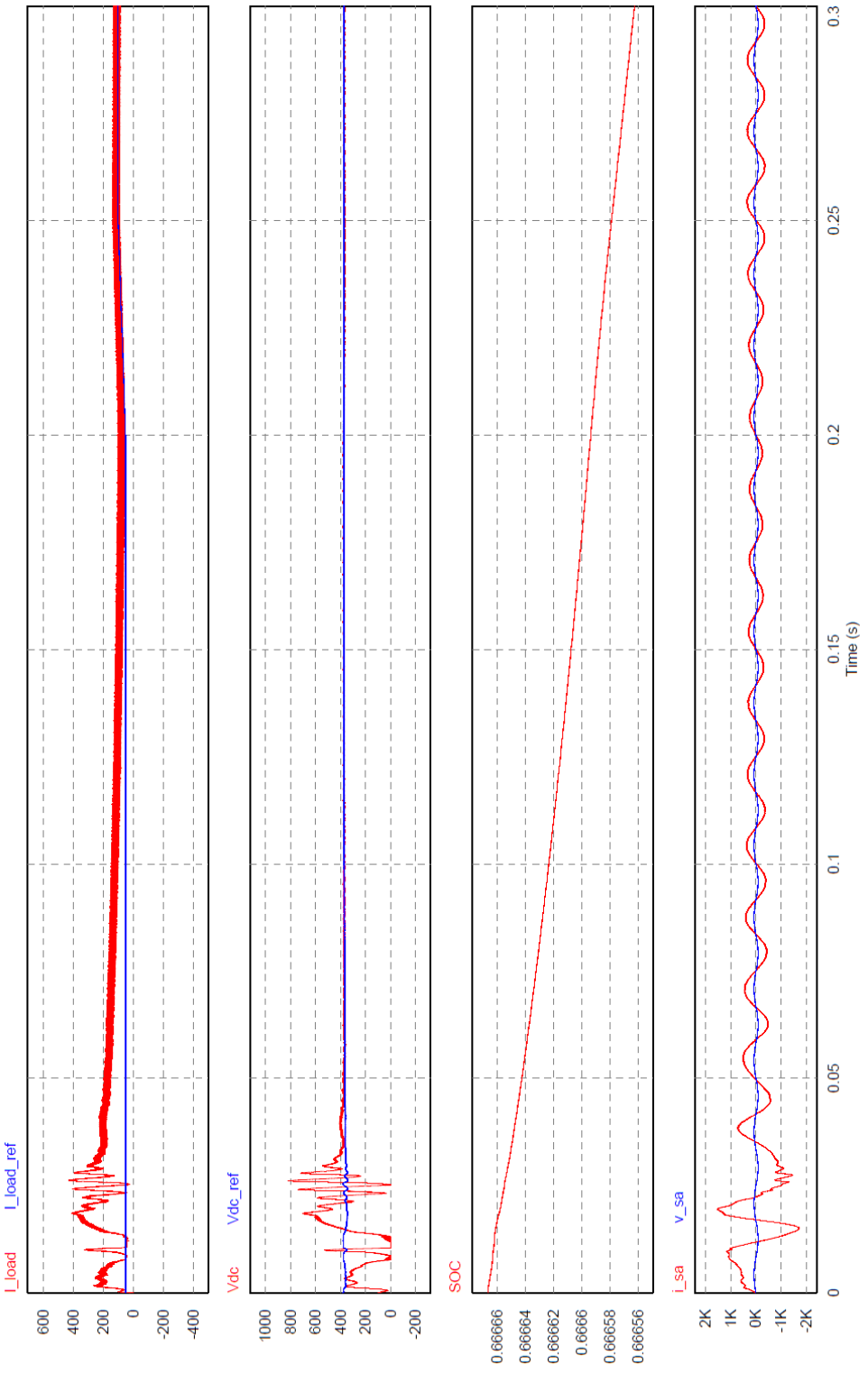

Figure 4-12 Zoom-in Plot of Simulation Result under Type I Design

4.2.2.2 Type II Design

By substituting parameters from Table 4-2 and Table 4-3 into (3-23) and (3-32), parameters for PI controller could be solved for as given in Table 4-5.

Table 4-5 Gains of PI Controllers under Type II Design

K_{ip}	0.00228284
K_{iI}	3.7712
K_{vp}	1.2914
K_{iI}	846.8196

The rest of the parameters are the same as those in type I design. Simulation results can be seen in Figure 4-13, Figure 4-14 and Figure 4-15, which indicates that the system under the type II tuning for PI controllers achieves the same tracking goals as with the system under type I tuning design in steady state.

From Figure 4-16, it can be seen that the system enters steady state before 0.05 seconds and the maximum transient load current I_{load} is approximately 1000 A while the maximum transient VSC output voltage V_{dc} is approximately 1300 V.

Comparing the two sets of results, one can see that under type II design, the system converges from transient state to steady state much faster than under type I design while the former system has much greater transient peak current and voltage than the latter system. These results are aligned with the studies for type I system and type II system in the appendices.

Type I and type II designs both satisfy the tracking requirements of the system in steady state while transient characteristics of these two designs show great differences. Therefore, to decide which tuning method to choose in a specific application, special circumstances have to be considered in order to avoid jeopardizing the system's safe operation while satisfying the requirements.

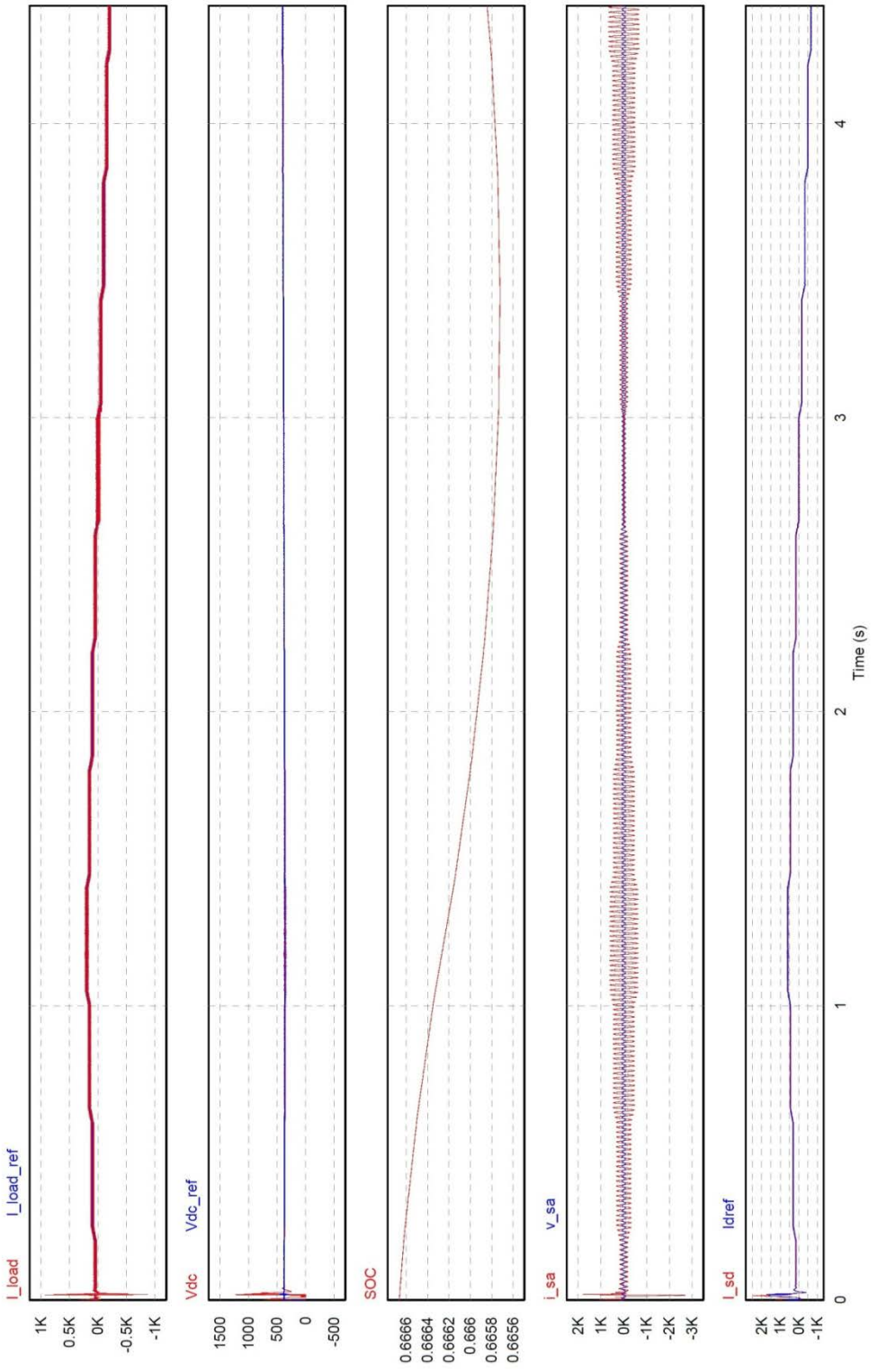

Figure 4-13 Simulation Results for VSC-Ideal Load Combination under Type II Design

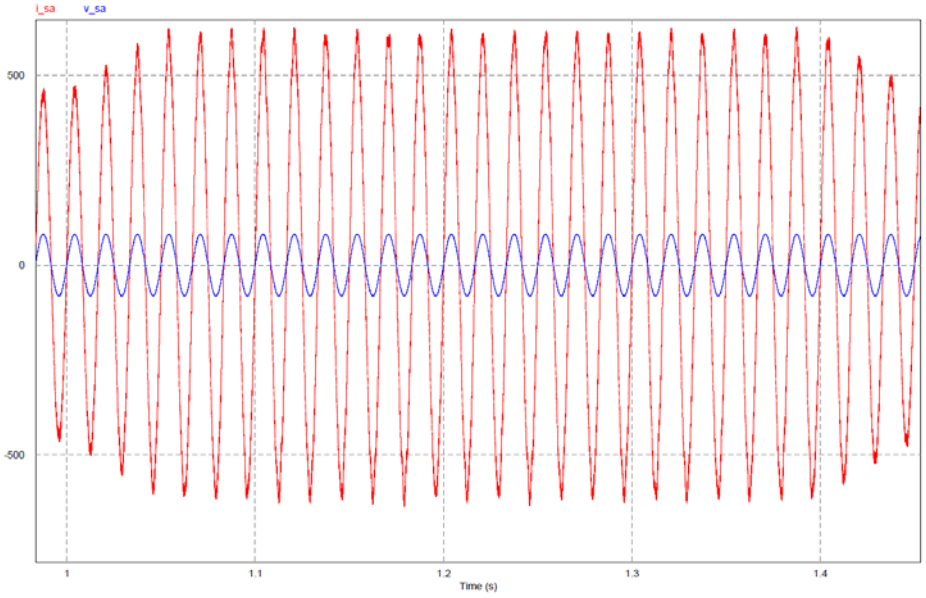

Figure 4-14 Zoomed-in Plot of Phase Voltage and Phase Current for Discharging State under Type II Design

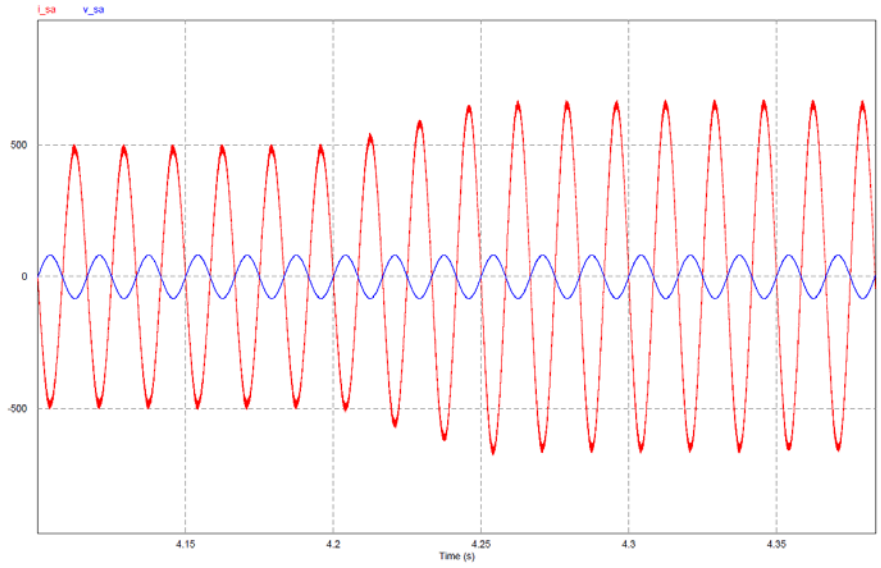

Figure 4-15 Zoomed-in Plot of Phase Voltage and Phase Current for Charging State under Type II Design

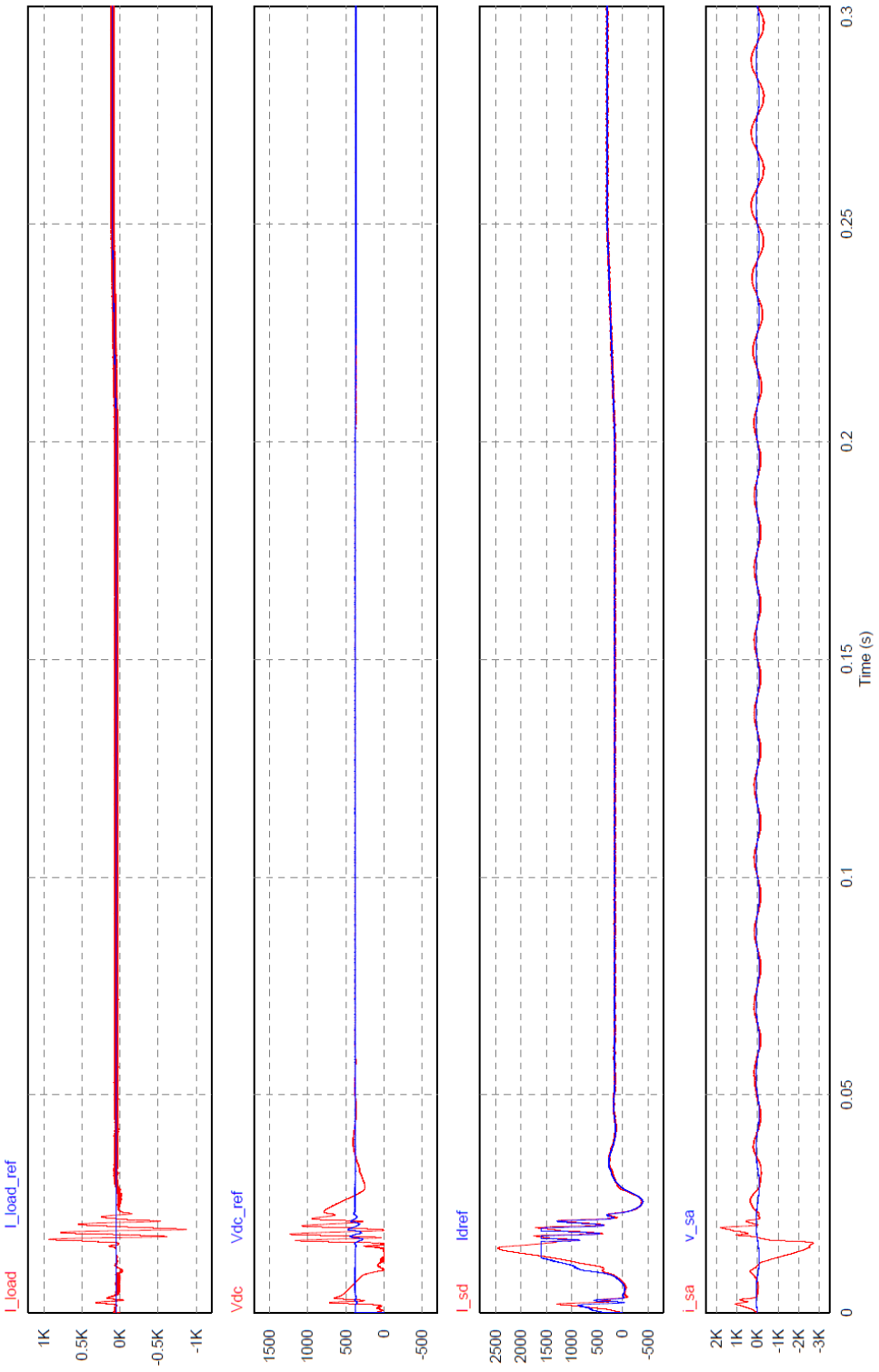

Figure 4-16 Zoom-in Plot of Simulation Result under Type II Design

4.3 Simulation of Battery Simulator with Motor Load

4.3.1 The Modeling of Motor Load System

The motor system PSIM model (shown in Figure 4-17) has been created by my supervisor and another MASc student (Martin Kadarsz). Generally, the system consists of a VSC to control power flow between the battery and the electric machine, an ac motor and the control system.

Similar to the VSC used in the battery emulator system, the currents in the three phases are transferred into d axis and q axis components by Park's Transformation. The current projection on d axis controls the magnetic flux, while the current projection on q axis controls the developed torque and thus the rotational speed of the motor. Revolution Per Minute (RPM) is used as the unit for the rotational speed. In the PSim realization of the motor system, a controllable-torque motor is used. The ACX-2043-1 type ac motor is used in the project.

The following table shows the working conditions of the ACX-2043-1 motor.

Table 4-6 Data for ACX-2043-1 Motor

RPM	Torque (Nm)	Power (kW)	Current (A)
0	70.5	0	300
787	64	5.3	256.2
1378	70.50	10	277.3
1935	50.42	10	260.3
2520	30.00	8	203.4
3424	17.50	6	155.4
3990	12.86	5	153.1

The current in the above table is acquired under the certain test voltage and may change for different input voltages for the motor. However, the peak current for different voltage input appears in the same RPM and torque condition which is 1378 RPM and 70.5 Nm torque. The condition of zero RPM and 70.5 Nm torque should be prevented. Therefore, the locked rotor current is not considered for designing the battery.

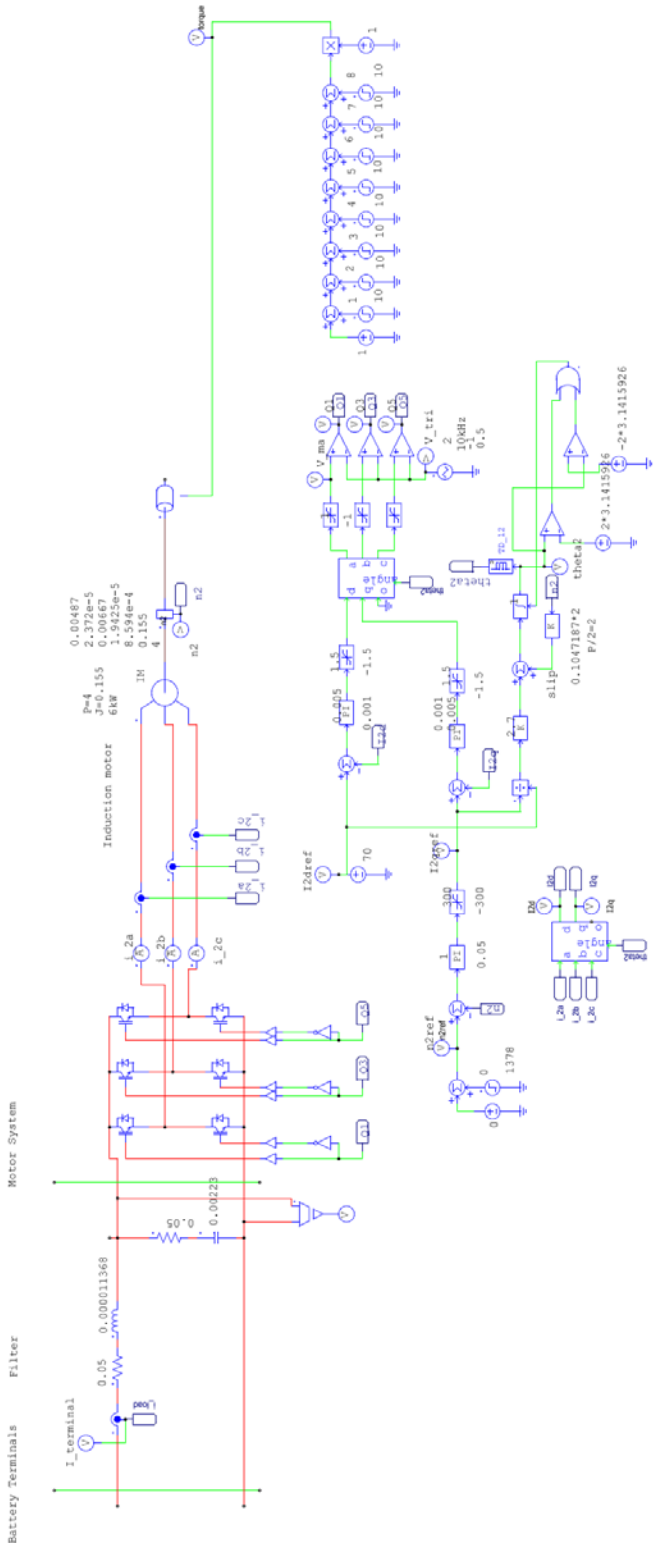

Figure 4-17 Circuit Diagram of Motor System

4.3.2 Design of Connection between VSC and Motor System

Since the motor system uses PWM switching technique, the current drawn from the dc side is not continuous while the battery circuit requires continuous input current to generate reference dc voltage. Therefore, RLC low pass filter is used to remove the ripples in the dc current.

The general Topology of RLC filter is shown in Figure 4-18.

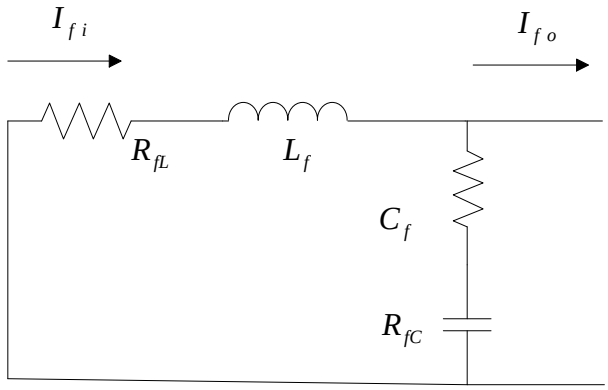

Figure 4-18 2nd Order RLC Filter

The transfer function of the filter is

$$F_f(s) = \frac{I_{fi}}{I_{fo}} = \frac{\frac{R_{fC}}{L_f}\left(s + \frac{1}{R_{fC}C_f}\right)}{s^2 + \frac{(R_{fL} + R_{fC})}{L_f}s + \frac{1}{L_f C_f}} = \frac{\frac{R_{fC}}{L_f}\left(s + \frac{1}{R_{fC}C_f}\right)}{s^2 + 2\xi_f \omega_r s + \omega_r{}^2} \tag{4-1}$$

According to the study of second order system shown in the Appendix C, the damping ratio, which usually set as 0.707, could be solved for as

$$\xi_f = \frac{(R_{fL} + R_{fC})}{2}\sqrt{\frac{C_f}{L_f}} \tag{4-2}$$

The resonant frequency, which usually set as one tenth of the switching frequency, could be solved as

$$f_r = \frac{\omega_r}{2\pi} = \frac{1}{2\pi}\sqrt{\frac{1}{L_f C_f}} \tag{4-3}$$

The filter resonant frequency in this work is chosen as 1,000 Hz since the switching frequency of the load is 10,000 HZ. Therefore, parameters of the filter could be solved for as given in Table 4-7.

Table 4-7 RLC Filter Design

$R_{fL} + R_{fC}$	C_f	L_f
0.001 Ω	0.2228 F	0.11368 μH
0.01 Ω	0.02228 F	1.1368 μH
0.1 Ω	0.002228 F	11.368 μH

The requirement for capacitance is too high if $R_{fL} + R_{fC}$ equals 0.001 Ω and 0.01 Ω. Therefore, 0.1 Ω is chosen for $R_{fL} + R_{fC}$. Higher R_{fL} means more power losses while higher R_{fC} causes more severe transients and voltage ripples. Therefore, a trade-off has been made by choosing $R_{fL} = R_{fC} = 0.05\,\Omega$.

4.3.3 Battery Simulator with Motor Load System

The input voltage for the motor system is rated at 96 V dc. Therefore, parameters for the battery circuit block are set as given in Table 4-8.

Table 4-8 C Block Parameters

Initial Ah	1.5
Nominal capacity	2.25
No. of Cells per branch	25
No. of Branches	69
Self-discharge current (A)	0.01

The parameters for the VSC are as given by Table 4-9.

Table 4-9 VSC Parameters

Ac Source line-line voltage (V)	50
Resistance per phase (Ω)	0.001
Inductance per phase (H)	0.0001
Capacitance on dc side (F)	0.0005

The same parameters for modulation are applied as given in Table 4-3. Previous simulation results for ideal load under type I design show that the system goes into steady state in less than 1 second, which is fast enough for the motor system to start. Type I design also produces much smaller peak current and peak voltage which is critical for the motor. Therefore, type I design is chosen as the tuning method for the system. The resulting PI controller parameters are given in Table 4-10.

Table 4-10 PI Controller Parameters

K_{ip}	0.004714
K_{iI}	0.04714
K_{vp}	1.2914
K_{iI}	846.8196

The circuit diagram of the overall system in PSim is shown in Figure 4-19.

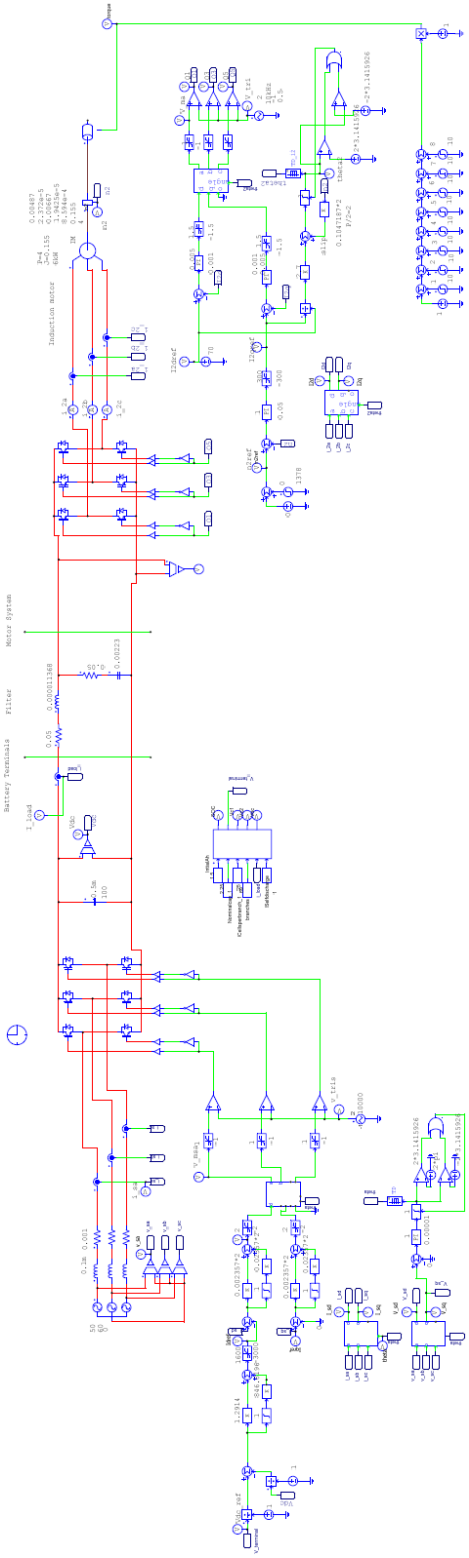

Figure 4-19 Battery Simulator integrated with Motor Load System

4.3.3.1 Positive Torque

With the mechanical load torque chosen as positive, the motor system only consumes power. The simulation results are shown in Figure 4-20 and Figure 4-21. A zoomed-in plot of phase voltage and phase current on the ac side of the emulator is shown in Figure 4-22.

Figure 4-20 and Figure 4-21 show that with the increase of RPM from 0 to 1378 and the increase of torque from 1 to 81 N.m, the current $I_{load\ ref}$ drawn from VSC increases from 0 to around 160 A while SoC decreases accordingly. The VSC output voltage V_{dc} successfully follows the reference voltage $V_{dc\ ref}$ generated by the battery model block, which proves the effectiveness of tuned parameters for the PI controller used in the outer voltage loop. The current on d axis i_{sd} successfully follows the reference signal i_{dref} generated by the outer voltage loop, which proves the effectiveness of the tuned parameters for the PI controller used in the inner current loop. The phase voltage v_{sa} on the ac side of emulator is a constant-magnitude sinusoidal voltage, while the phase current i_{sa} increases with the increase of power consumed by the motor system.

Figure 4-22 shows that i_{sa} and v_{sa} are strictly in phase with each other which proves the battery simulator system operates as expected at unity power factor at the grid interface. No giant distortion on ac current is observed.

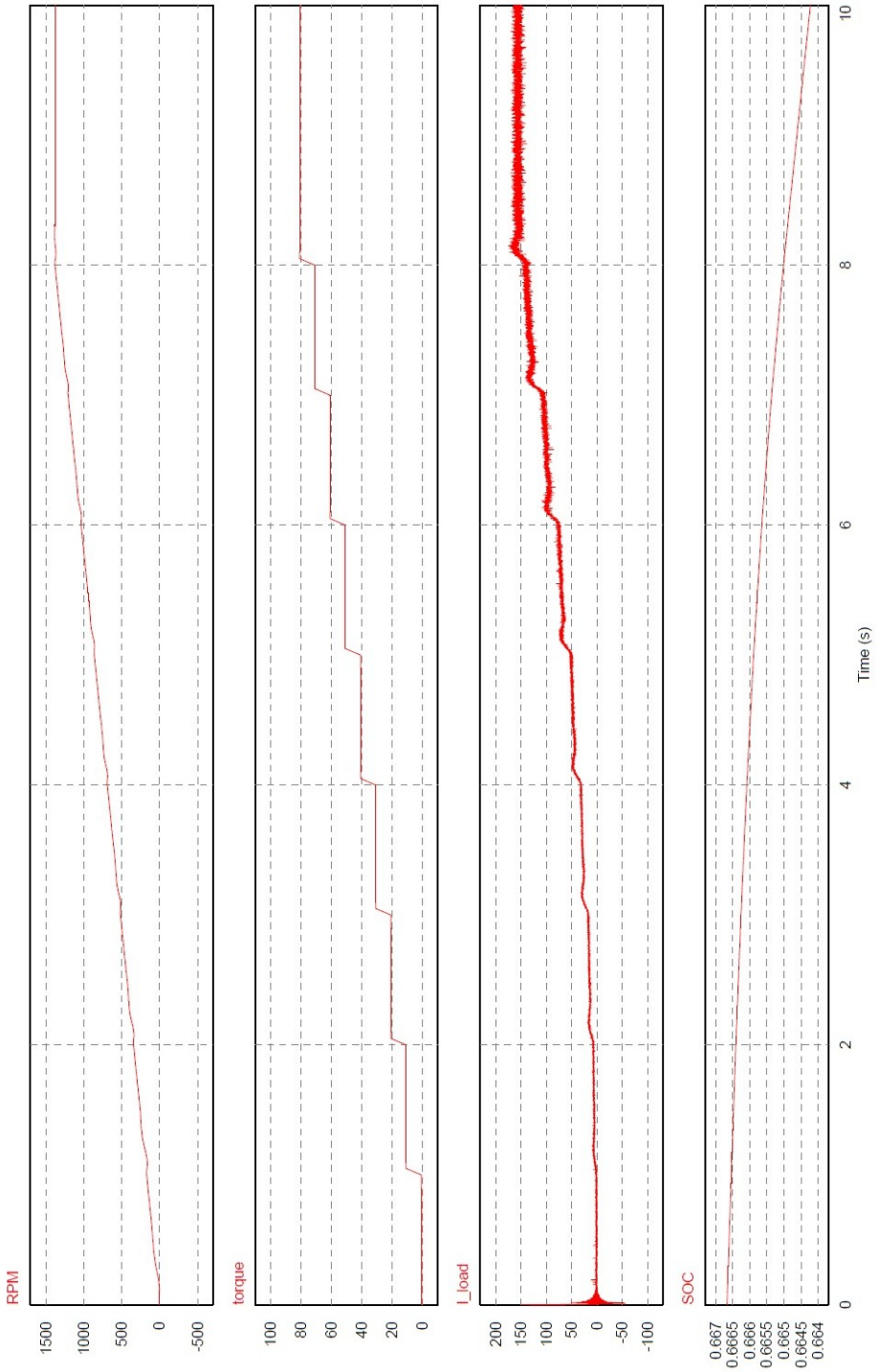

Figure 4-20 Simulation Result for Motor System Load with Positive Torque (I)

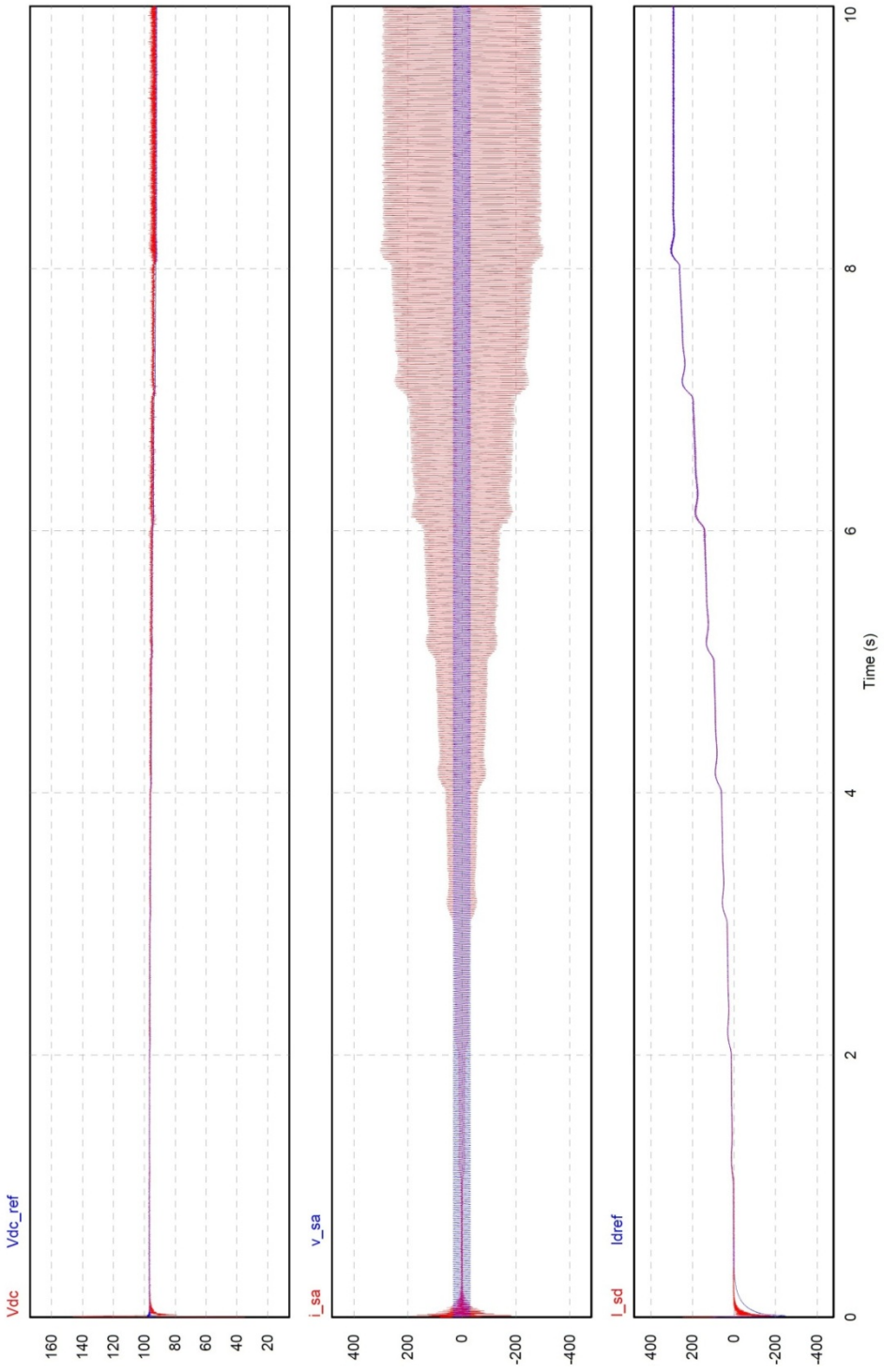

Figure 4-21 Simulation Result for Motor System Load with Positive Torque (II)

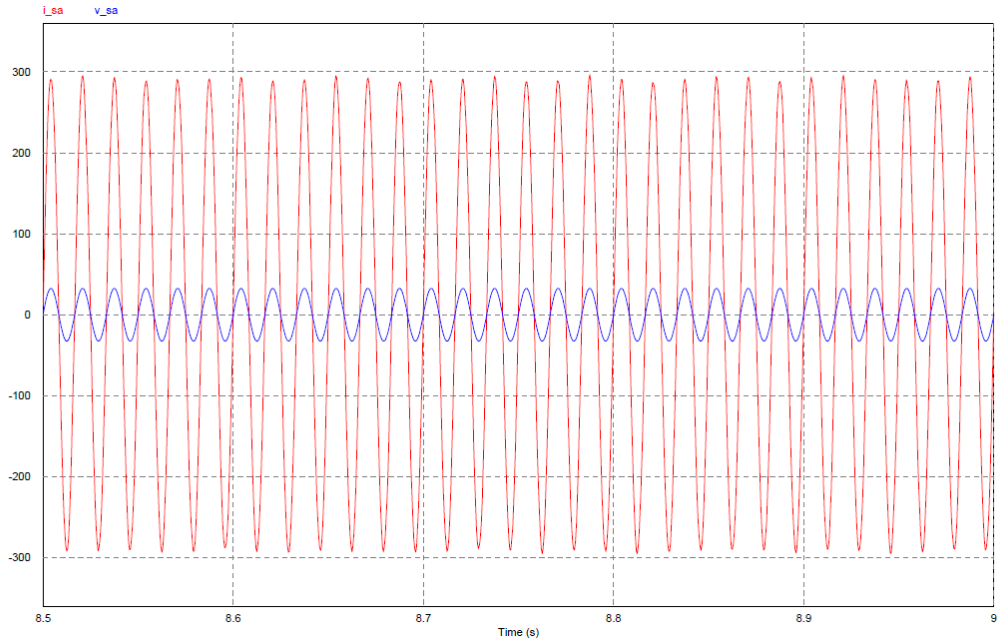

Figure 4-22 Zoomed-in Plot of Phase Voltage and Phase Current for Motor System Load with Positive Torque

4.3.3.2 Negative Torque

With the mechanical load torque chosen as negative, the motor system operates as a generator. The related simulation results are shown in Figure 4-23 and Figure 4-24. A zoomed-in plot of phase voltage and phase current on the ac side of the simulator is shown in Figure 4-25.

Figure 4-23 and Figure 4-24 show that with an increase in speed from 0 to 1378 rpm, and a change in torque from -1 to -81 N.m, the current $I_{load\ ref}$ drawn from VSC changes from 0 to around -100 A, while SoC increases accordingly. The VSC output voltage V_{dc} successfully follows the reference voltage $V_{dc\ ref}$, generated by the battery model block, while the d-axis current i_{sd} successfully follows the reference signal i_{dref} , generated by the outer voltage loop.

Figure 4-25 shows that i_{sa} and v_{sa} has 180 degrees phase shift with respect to each other, which proves the battery simulator system operates as expected by sending power to the grid. No considerable distortion in the ac current is observed.

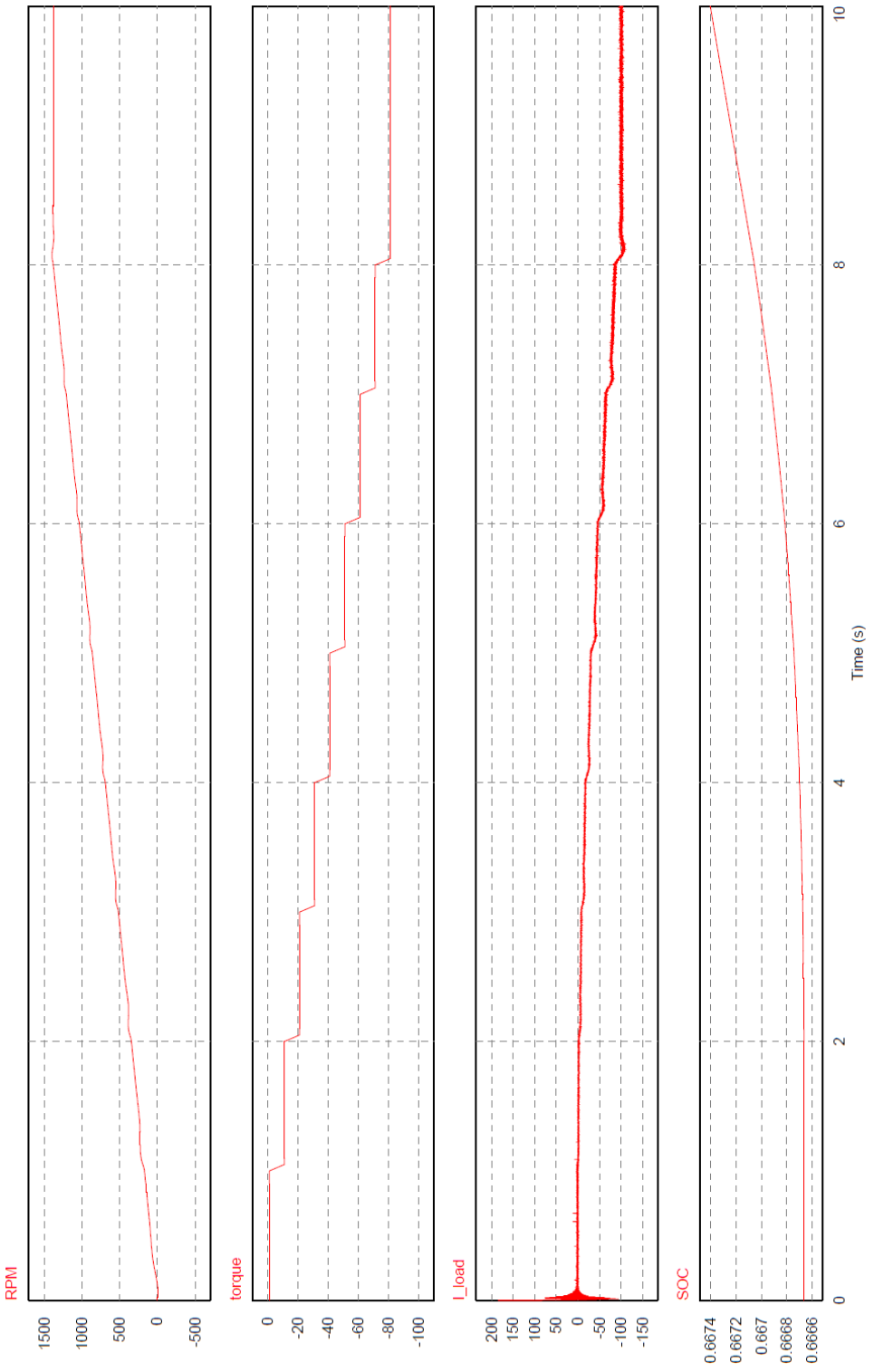

Figure 4-23 Simulation Results for Motor System Load with Negative Torque (I)

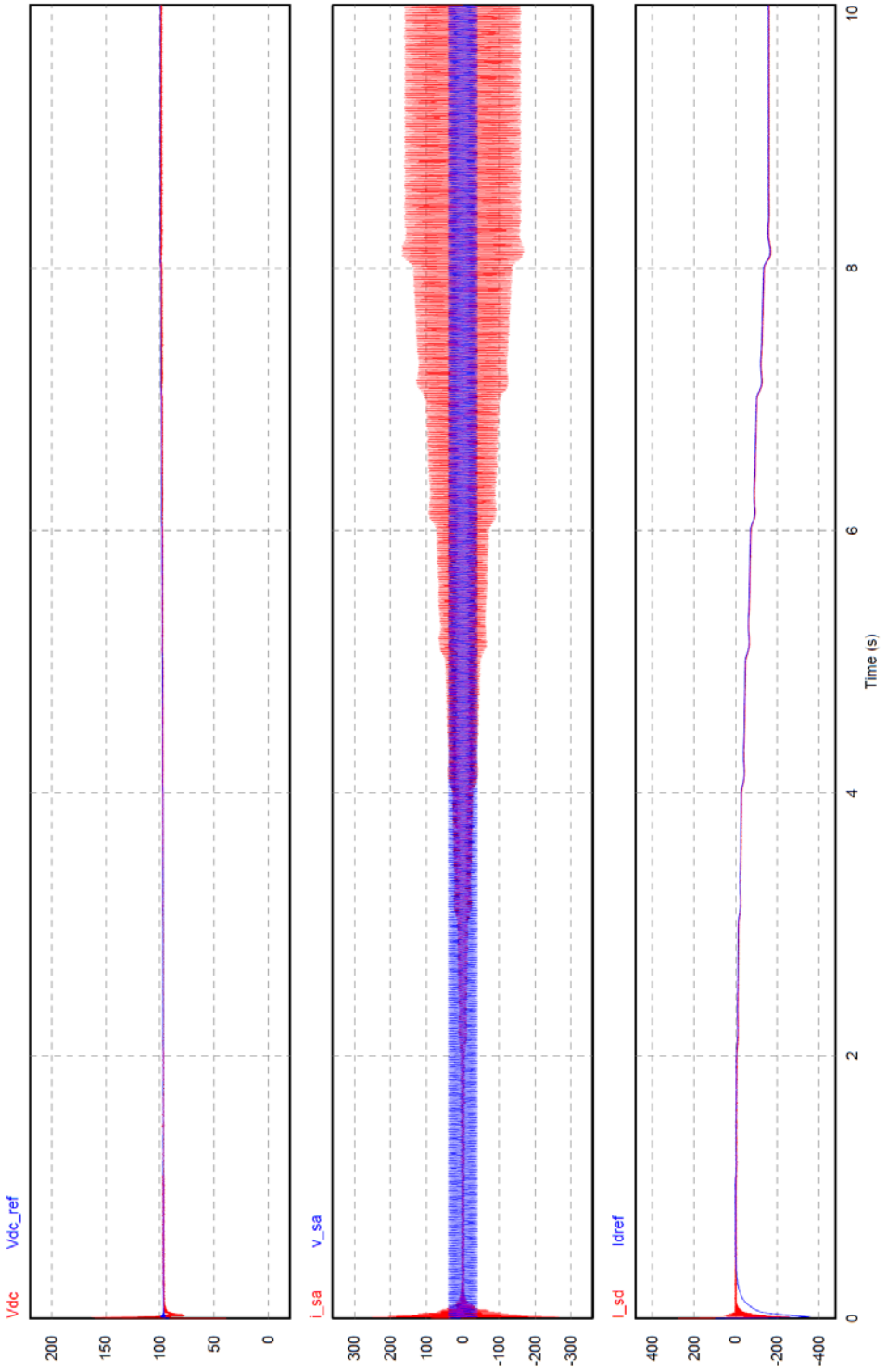

Figure 4-24 Simulation Results for Motor System Load with Negative Torque (II)

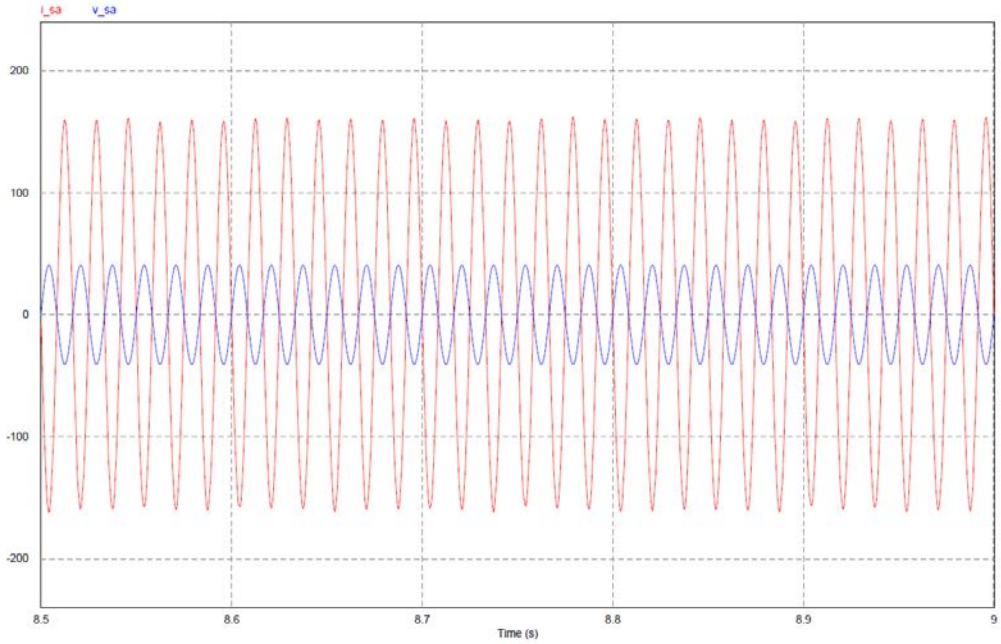

Figure 4-25 Zoomed-in Plot of Phase Voltage and Phase Current for Motor System Load with Negative Torque

4.3.3.3 Transition from Positive Torque to Negative Torque

With the sign of mechanical load torque changing from positive to negative, the electric machine changes mode from motoring (power consumption) to generating (power generation). The corresponding simulation results are shown in Figure 4-26 and Figure 4-27. Zoomed-in plots of phase voltage and phase current on the ac side of the simulator are shown in Figure 4-28 and Figure 4-29 for positive and negative load torque, respectively.

Figure 4-26 and Figure 4-27 show that with an increase of speed from 0 to 1378 rpm, and the torque change from 1 to 31 N.m and then from 31 to -29 N.m, the current $I_{load\ ref}$ drawn from VSC increases from 0 to around 32 A and then decreases from 32 to around -40 A, while SoC decreases and increases accordingly. The VSC output voltage V_{dc} successfully follows the reference voltage $V_{dc\ ref}$, generated by the battery model block, while the d-axis current i_{sd} successfully follows the reference signal i_{dref}, generated by the outer voltage loop.

Figure 4-28 shows that i_{sa} and v_{sa} are strictly in phase with each other which proves the battery simulator system operates as expected at unity power factor at the grid interface while the torque is positive; Figure 4-29 shows that i_{sa} and v_{sa} have 180 degrees phase shift with respect to each other, which proves the battery simulator system operates as expected by sending power to the grid while the torque is negative. No noticeable distortion in the ac current is observed.

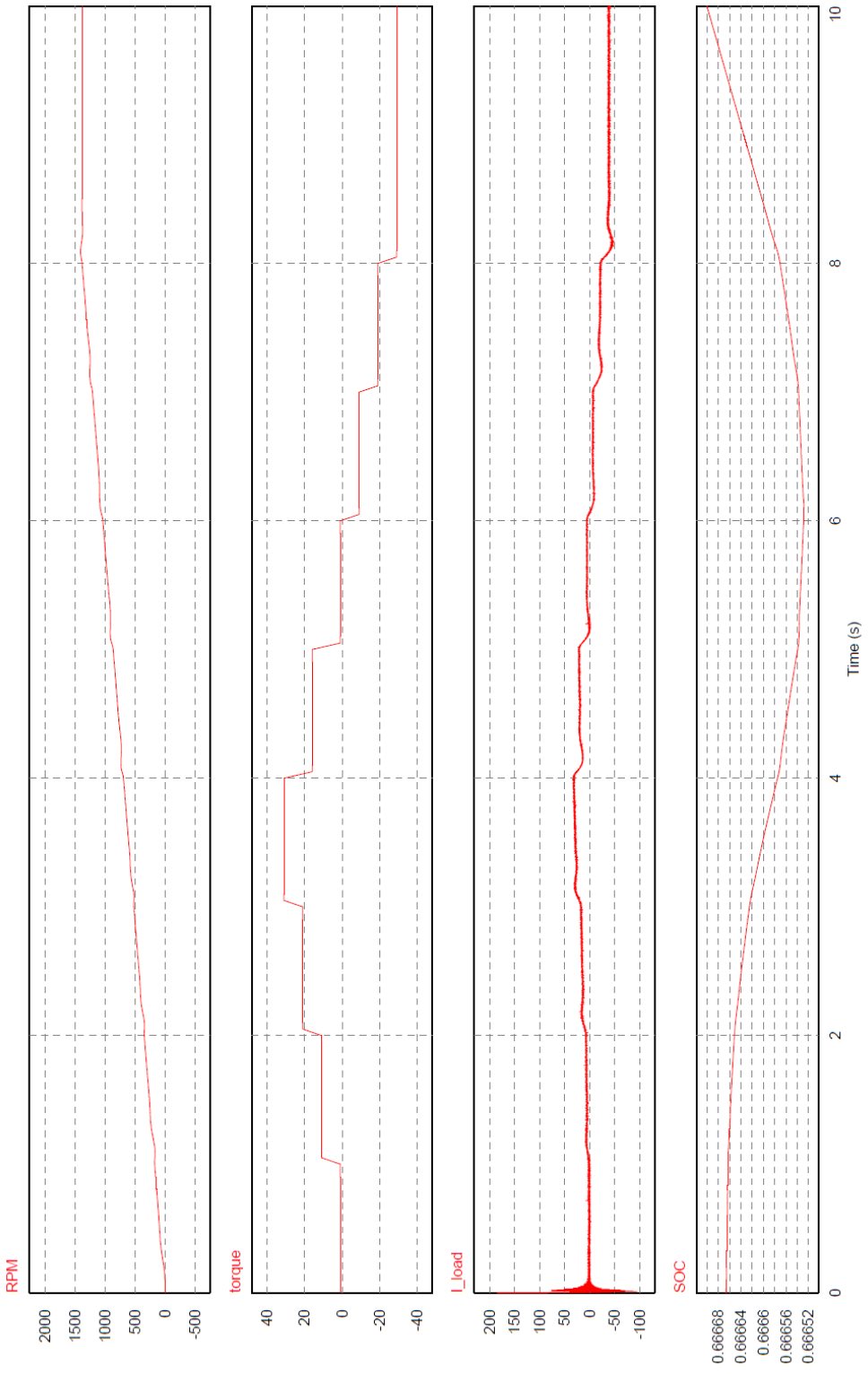

Figure 4-26 Simulation Results for Motor System Load with Variable Torque (I)

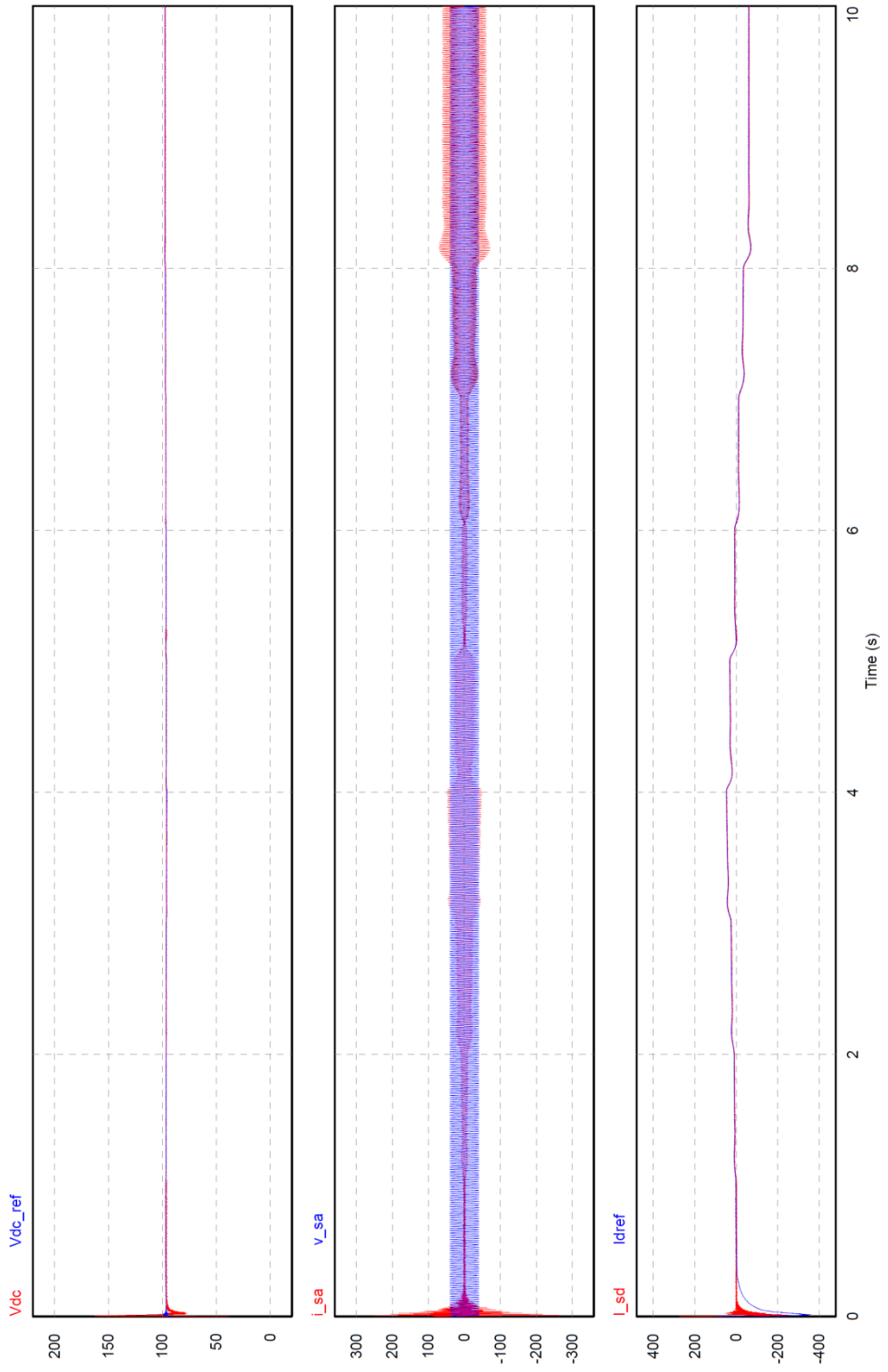

Figure 4-27 Simulation Results for Motor System Load with Variable Torque (II)

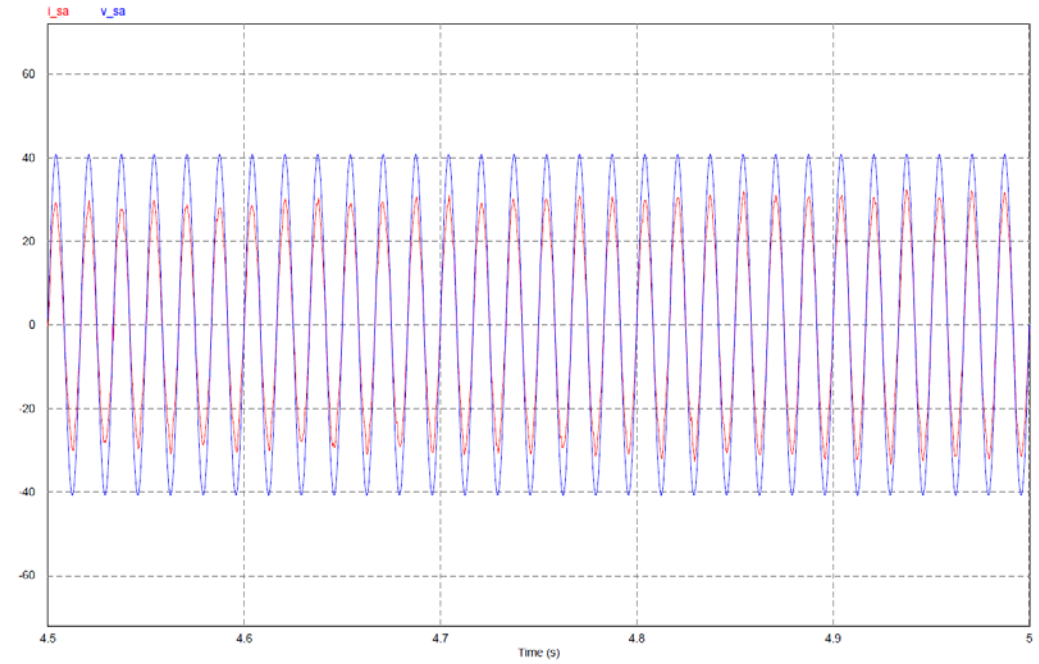

Figure 4-28 Zoomed-in Plot of Phase Voltage and Phase Current for Motor System Load with Variable Torque (I)

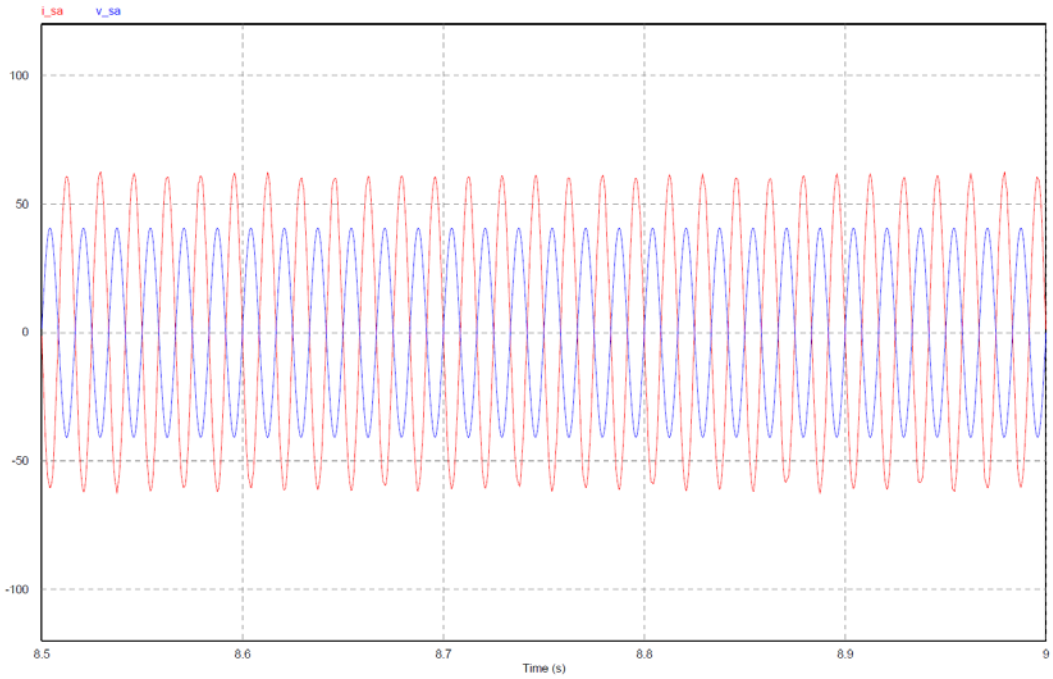

Figure 4-29 Zoomed-in Plot of Phase Voltage and Phase Current for Motor System Load with Variable Torque (II)

Chapter 5
Conclusions

5.1 Summary

Chapter 1 presents the study of the future market for electrical vehicles, showing growing demand for EVs. Such trend creates great need for vehicle design, development and testing, creating huge potential for use of battery simulators, due to high cost of actual batteries. Battery simulators are supposed to be capable of providing a high power supply and emulating multiple types of battery cells during the developing process of new EVs, HEVs and PHEVs. However, survey of existing battery simulators finds that majority of products in stock could hardly satisfy the above two requirements. Therefore, creating a high-performance battery simulator that is able to withstand high power demand, while emulating different cell types, is motivated by this gap.

Chapter 2 overviews and compares the battery models proposed by researchers, and studies the modelling methods for VSC. The VSC model in abc frame is discussed to study the stability of the system, while the VSC model in dq frame is applied to simplify the control strategy due to decoupling offered by this approach.

Based on the work reported in Chapter 2, a new battery simulator structure is proposed in Chapter 3 by picking an electrical circuit model for the battery from the models discussed in Chapter 2 and creating a cascaded control scheme for the VSC based on the dq frame. A tuning technique for the PI controllers utilized in the VSC is presented according to the block diagram of the control loop. Realization of the battery model and the VSC are presented in this chapter.

Chapter 4 gives the simulation results for the two realizations of battery simulator model which proves the accuracy of both approaches. The battery simulator used a C block to generate reference signal for VSC, with an ideal load and a realistic motor system load. The ideal load proves the battery simulator's capability of working with high power and the motor system load proves the battery simulator's ability to withstand high ripples in the load current in the real case.

5.2 Contributions

The main contributions of this thesis is development of a battery simulator capable of realizing different sizes of battery pack, emulating battery packs made of multiple types of battery cells and working under different loading conditions.

5.3 Future Work

Some simplifications have been made in the course of the work on realization of the electrical circuit battery model by ignoring the cycle number-dependent correction factor and temperature-dependent correction factor when calculating the capability of the battery cell. These factors need to be considered for more precise I/O characteristics of battery cells in the battery simulator.

Appendix A

Matlab Code for Producing Transfer Functions based on the Small-Signal Linearized Model of VSC

The Creation of Transfer Functions in General Forms

```
syms Vdc M Im s C L R Em Iload
B=[-Vdc/2/L, 0
    0, -M*Vdc/(2*L*Im)
    0.75*Im/C, 0];
A=[-R/L, 0, -M/(2*L)
    0, M*Vdc/(2*L*Im)-Em/(L*Im),0
    0.75*M/C, 0, -Iload/(Vdc*C)];
C1=[0,0,1];
C2=[0,1,0];
C3=[1,0,0];
I=[1, 0, 0
    0, 1, 0
    0, 0, 1];
trans1=C1*(s*I-A)^(-1)*B(:,1);
trans2=C1*(s*I-A)^(-1)*B(:,2);
trans3=C2*(s*I-A)^(-1)*B(:,1);
trans4=C2*(s*I-A)^(-1)*B(:,2);
trans5=C3*(s*I-A)^(-1)*B(:,1);
trans6=C3*(s*I-A)^(-1)*B(:,2);
[trans11, trans12] = numden(sym(trans1));
[trans21, trans22] = numden(sym(trans2));
[trans31, trans32] = numden(sym(trans3));
[trans41, trans42] = numden(sym(trans4));
[trans51, trans52] = numden(sym(trans5));
[trans61, trans62] = numden(sym(trans6));
```

Transfer Functions under Specified Conditions

```
syms s C s1 s2 s3 s4 s5 s6 M
Vdc=95;
```

```
%M=1;
Im=186.16;
L=0.1*0.001;
R=0.001;
Em=50*sqrt(2);
Iload=120;
trans11 =6*Im*R*Vdc - 3*M*Vdc^2 + 6*Im*L*Vdc*s
trans12 =3*M^2*Vdc + 8*Iload*R + 8*Iload*L*s + 8*C*L*Vdc*s^2 + 8*C*R*Vdc*s
trans41 =-M*Vdc
trans42 =2*Em - M*Vdc + 2*Im*L*s
trans51 =- 4*Iload*Vdc - 3*Im*M*Vdc - 4*C*Vdc^2*s
trans52 =3*M^2*Vdc + 8*Iload*R + 8*Iload*L*s + 8*C*L*Vdc*s^2 + 8*C*R*Vdc*s
```

Appendix B
Code for C block in PSim

Variable/Function Definitions

```
#include <Stdlib.h>
#include <String.h>


 int g_nInputNodes=0;
 int g_nOutputNodes=0;

 int g_nStepCount=0;

float buffer1=0.0;
float buffer2=0.0;
float buffer3=0.0;
float buffer4=0.0;
float Vc1=0.0;
float Vc2=0.0;
```

OpenSimUser Fcn

```
void OpenSimUser(const char *szId, const char * szNetlist, int nInputCount, int nOutputCount, int
*pnError, char * szErrorMsg)
{
g_nInputNodes = nInputCount;
 g_nOutputNodes = nOutputCount;


// In case of error, uncomment next two lines. Set *pnError to 1 and copy Error message to
szErrorMsg
 //*pnError=1;
 //strcpy(szErrorMsg, "Place Error description here.");
```

```
}
```

RunSimUser Fcn

```
void RunSimUser(double t, double delt, double *in, double *out, int *pnError, char * szErrorMsg)
{
g_nStepCount++;

// In case of error, uncomment next two lines. Set *pnError to 1 and copy Error message to
szErrorMsg
 //*pnError=1;
 //strcpy(szErrorMsg, "Place Error description here.");

float SOC, Voc, R, R1, R2, C1, C2;

buffer1+=in[4]*delt;
   buffer3=buffer1/in[3];

   buffer2+=in[5]*delt;



   SOC=(in[0]-(buffer3+buffer2)/3600)/in[1];
   out[0]=SOC;
   Voc=in[2]*((-1.031*exp(-35*SOC))+(3.685)+(0.2156*SOC)-
(0.1178*SOC*SOC)+(0.3201*SOC*SOC*SOC));

   R=in[2]/in[3]*(0.1562*exp(-24.37*SOC)+0.07447);
   R1=in[2]/in[3]*(0.3208*exp(-29.14*SOC)+0.04669);
   R2=in[2]/in[3]*(6.603*exp(-155.2*SOC)+0.04984);
   C1=in[3]/in[2]*(-752.9*exp(-13.51*SOC)+703.6);
   C2=in[3]/in[2]*(-6056*exp(-27.12*SOC)+4475);
   Vc1=(R1*delt*in[4]+C1*R1*Vc1)/(delt+R1*C1);
   Vc2=(R2*delt*in[4]+C2*R2*Vc2)/(delt+R2*C2);
```

```
    out[2]=Vc1;
    out[3]=Vc2;
    out[1]=Voc-Vc1-Vc2-in[4]*R;
    out[4]=Voc;

}
```

Appendix C

Study of Type I and Type II Systems

In this section, the design criteria for type I and II systems [34] will be specified. The open-loop transfer function of the system can be generally written as

$$W(s) = \frac{K\prod_{i=1}^{m}(\tau_i^* s+1)}{s^r\prod_{j=1}^{n}(T_j^* s+1)} \tag{C-1}$$

The value of r defines the number associated with the type of the system. For example, if $r=0$, the system is Type 0; if $r=1$, the system is Type I; and if $r=2$, the system is Type II.

The Study of Type I System

The open-loop transfer function of a typical type I system can be written as

$$W(s)_I = \frac{K}{s(T^* s+1)} \tag{C-2}$$

where

T^* is the inertia time constant of the system; and

K is the gain of the open-loop system

The ideal bode diagram of the open-loop system, in which the curve crosses 0 dB with the slope of -20 dB/dec, can be drawn as shown in Figure C- 1

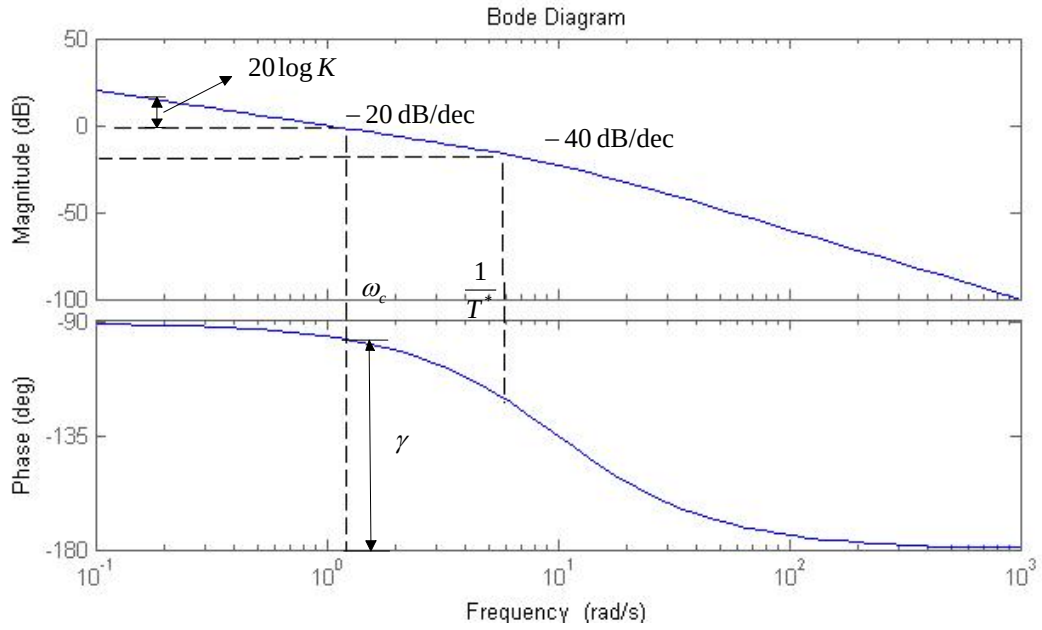

Figure C- 1

From above figure, when $\omega_c < \frac{1}{T^*}$, one can write

$$20\log K = 20(\log \omega_c - \log 1) = 20\log \omega_c \tag{C-3}$$

Therefore, when $\omega_c < \frac{1}{T^*}$,

$$K = \omega_c \tag{C-4}$$

The phase margin γ can be solved for as

$$\gamma = 180^\circ - 90^\circ - \arctan \omega_c T^* = 90^\circ - \arctan \omega_c T^* \tag{C-5}$$

Since $\omega_c < \frac{1}{T^*}$, $T^*\omega_c < 1$. Hence,

$$\arctan \omega_c T^* < 45^\circ \tag{C-6}$$

By substituting (C-6) into (C-5), it can be concluded that the phase margin γ is greater than 45 degree. In other words, the system has sufficient phase margin to be considered stable.

The close-loop transfer function of the system is

$$W(s)_{Close\ I} = \frac{W(s)_I}{1+W(s)_I} = \frac{\frac{K}{T^*}}{s^2 + \frac{1}{T^*}s + \frac{K}{T^*}} = \frac{\omega_n^2}{s^2 + 2\xi\omega_n s + \omega_n^2} \tag{C-7}$$

where

ω_n is the natural frequency of the system which is defined as

$$\omega_n = \sqrt{\frac{K}{T^*}} \tag{C-8}$$

ξ is the damping ratio which is defined as

$$\xi = \frac{1}{2}\sqrt{\frac{1}{KT^*}} \tag{C-9}$$

The type I system is a second order system. When $\xi < 1$, the system is under-damped; when $\xi > 1$, the system is over-damped; and when $\xi = 1$, the system is critically-damped. In order to have a fast dynamic response, the system works in the under-damped mode. Under such conditions, the overshoot σ of the system can be solved for as

$$\sigma = e^{-(\xi\pi/\sqrt{1-\xi^2})} \times 100\% \tag{C-10}$$

The rise time t_r of the system is

$$t_r = \frac{2\xi T^*}{\sqrt{1-\xi^2}}\left(\pi - \cos^{-1}(\xi)\right) \tag{C-11}$$

The peak time t_p of the system is

$$t_p = \frac{\pi}{\omega_n\sqrt{1-\xi^2}} \tag{C-12}$$

The cutoff frequency ω_c is

$$\omega_c = \omega_n[\sqrt{4\xi^4+1} - 2\xi^2]^{0.5} \tag{C-13}$$

The phase margin γ is

$$\gamma = \arctan \frac{2\xi}{\left[\sqrt{4\xi^4 + 1} - 2\xi^2\right]^{0.5}} \tag{C-14}$$

According to the above equations, Table C- 1 has been produced.

Table C- 1 Parameters of Type I System

KT^*	0.25	0.39	0.50	0.69	1.0
Damping Ratio ξ	1.0	0.8	0.707	0.6	0.5
Overshoot σ	0%	1.5%	4.3%	9.5%	16.3%
Rise Time t_r		$6.6T^*$	$4.7T^*$	$3.3T^*$	$2.4T^*$
Peak Time t_p		$8.3T^*$	$6.2T^*$	$4.7T^*$	$3.6T^*$
Phase Margin γ	76.3°	69.9°	65.5°	59.2°	51.8°
Cutoff Frequency ω_c	$0.243/T^*$	$0.367/T^*$	$0.455/T^*$	$0.596/T^*$	$0.786/T^*$

From Table C- 1, it can be seen that

a. If faster response is required, damping ratio could be set between 0.5 and 0.6 to have a greater value for KT^*.

b. If smaller over shoot is required, damping ratio could be set between 0.8 and 1 to have a smaller value for KT^*.

c. Damping ratio of 0.707 is a good trade-off between over shoot and response speed. Under such circumstances, over shoot and response speed are in the mid-range.

The Study of Type II System

The open-loop transfer function of a typical type II system can be written as

$$W(s)_{II} = \frac{K(\tau^* s + 1)}{s^2(T^* s + 1)} \tag{C-15}$$

The ideal bode diagram of the open-loop system, in which the curve crosses 0 dB with the slope of -20 dB/dec, can be drawn as shown in Figure C- 2

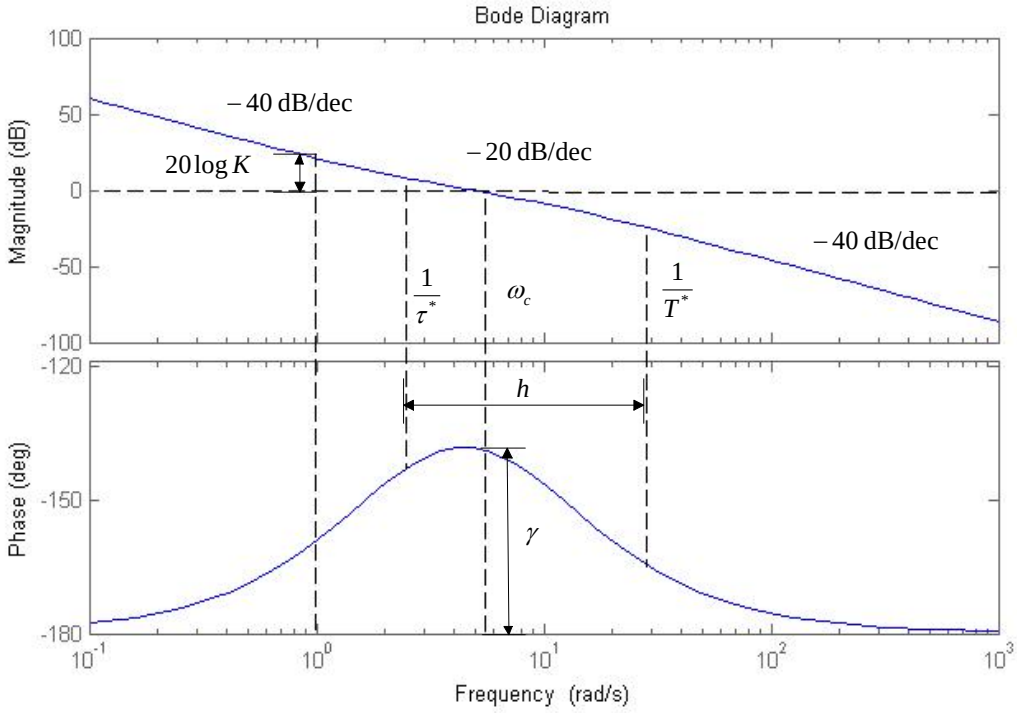

Figure C- 2

The role of $(\tau^* s+1)$ is to raise the phase curve above -180 degree in order to leave sufficient phase margin to keep the system stable. To realize the ideal diagram shown above, the following condition has to be satisfied

$$\frac{1}{\tau^*} < \omega_c < \frac{1}{T^*} \tag{C-16}$$

or

$$\tau^* > T^* \tag{C-17}$$

The phase margin γ can be calculated as

$$\gamma = 180^\circ - 180^\circ + \arctan \omega_c \tau^* - \arctan \omega_c T^* = \arctan \omega_c \tau^* - \arctan \omega_c T^* \tag{C-18}$$

(C-18) shows that the greater the difference between τ^* and T^*, the more stable the system is.

The bandwidth of 20 dB/dec, which is critical for the control, can be defined as

$$h = \frac{\tau^*}{T^*} = \frac{\omega_2}{\omega_1} \tag{C-19}$$

Since the point $\omega = 1$ lies on the curve with -40 dB/dec slope,

$$20\log K = 40(\log\omega_1 - \log 1) + 20(\log\omega_c - \log\omega_1) = 20\log\omega_1\omega_c \tag{C-20}$$

Therefore,

$$K = \omega_1\omega_c \tag{C-21}$$

From equation (C-21), it can be seen that if T^* is a constant value, changing τ^*, which is the inverse of ω_1, changes the bandwidth of the middle frequency (-20 dB/dec); Once τ^* is set, changing K changes the cutoff frequency ω_c.

To have the minimum close-loop frequency response of the system, the 'optimal relation' for ω_1, ω_2 and ω_c could be concluded as

$$\frac{\omega_2}{\omega_c} = \frac{2h}{h+1} \tag{C-22}$$

$$\frac{\omega_c}{\omega_1} = \frac{h+1}{2} \tag{C-23}$$

From equation (C-22) and (C-23), K could be solved for as

$$K = \omega_1\omega_c = \frac{h+1}{2h^2T^{*2}} \tag{C-24}$$

From equation (C-19), τ^* can be solved for as

$$\tau^* = hT^* \tag{C-25}$$

By substituting (C-24) and (C-25) into the open-loop transfer function (C-15), one gets

$$W(s)_{II} = \left(\frac{h+1}{2h^2T^{*2}}\right)\frac{hT^*s+1}{s^2(T^*s+1)} \tag{C-26}$$

The closed-loop transfer function can be derived as

$$W(s)_{Close\ II} = \frac{W(s)_{II}}{1+W(s)_{II}} = \frac{hT^*s+1}{\frac{2h^2}{h+1}T^{*3}s^3 + \frac{2h^2}{h+1}T^{*2}s^2 + hT^*s+1} \quad \text{(C-27)}$$

Let $W(s)_{Close\ II} = \frac{C(s)}{R(s)}$, where $R(s)$ is unit step function which can be written as $R(s) = \frac{1}{s}$. $C(s)$ can be represented as

$$C(s) = \frac{hT^*s+1}{s\left(\frac{2h^2}{h+1}T^{*3}s^3 + \frac{2h^2}{h+1}T^{*2}s^2 + hT^*s+1\right)} \quad \text{(C-28)}$$

Setting T^* as a constant number while changing the value of h, (C-28) can be utilized to calculate the unit step response function $C(t/T^*)$, from which the overshoot σ, rise time t_r, peak time t_p and numbers of oscillation k can be calculated as shown in Table C- 2.

Table C- 2 Overshoot σ, Rise time t_r, Peak time t_p and Numbers of Oscillation k

h	3	4	5	6	7	8	9
σ	52.5%	43.6%	37.6%	33.2%	29.8%	27.2%	25.0%
t_r	2.40	2.65	2.85	3.0	3.1	3.2	3.3
t_p	12.15	11.65	9.55	10.45	11.30	12.25	13.25
k	3	2	2	1	1	1	1

Table C- 2 shows that

a. The settling time does not change monotonically with the increase of h. When $h=5$, the system has the shortest settling time.

b. With the increase of h, the overshoot decreases.

c. $h=5$ satisfies the requirement of smallest settling time while overshoot is in the middle of its range

Compare Table C- 1 and Table C- 2, it can be deducted that type II system converges to the steady state faster, while type I system has much smaller overshoot during transient period.

Bibliography

[1] Clean Energy Ministerial, Electric Vehicle Initiative and International Energy Agency, "Global EV Outlook-Understanding the Electric Vehicle Landscape to 2020 ", April 2013. [Online]. Available: https://www.iea.org/publications/globalevoutlook_2013.pdf

[2] Nissan Motor Company Ltd, "The new car: features and specifications", 2011, [Online]. Available:http://www.nissanusa.com/electric-cars/leaf/#/leaf-electric-car/specs-features/index

[3] Tesla Motors Inc., "Roadster Technology- Battery", [Online]. Available: https://www.tesla-motors.com/roadster/technology/battery

[4] U.S Department of Energy, "Batteries for Hybrid and Plug-In Electric Vehicles", [Online], Available: http://www.afdc.energy.gov/vehicles/electric_batteries.html

[5] Ametek Inc., "Ametek Programmable Power", [Online]. Available: http://www.progr-ammable power.com/dc-power-supply/DLM600/Specifications.htm

[6] Bloomy Inc., "Battery Simulator 1200", [Online]. Available: http://www.bloomy.com/ pro-ducts/battery-management-system-testing/battery-simulator-1200#tabs=1

[7] Tektronix Inc., "Tektronix and Keithley DC Power Supply", [Online]. Available: http://www.tek.com/dc-power-supply

[8] M. Chen and G. A. Rincon-Mora, "Accurate Electrical Battery Model Capable of Predicting Runtime and I–V Performance." *IEEE Trans. Energy Conversion*, vol. 21(2), pp. 504-511, June 2006

[9] R. Rao, S. Vrudhula, D. N. Rakhmatov, "Battery Modeling for Energy-Aware System Design," *IEEE Computer*, vol. 36 (12), pp. 77 – 87, Dec.3 2003

[10] M. Pedram and Q. Wu, "Design Considerations for Battery-Powered Electronics," *in Proc. 1999 IEEE Design Automation Conference*, pp. 861-866

[11] H. L. Chan and D. Sutanto, "A New Battery Model for use with Battery Energy Storage Systems and Electric Vehicles Power Systems," *in Proc. 2000 IEEE Power Engineering Society Winter Meeting*, pp.470-475

[12] K. C. Syracuse and W. D. K. Clark, "A Statistical Approach to Domain Performance Modeling for Oxyhalide Primary Lithium Batteries," *in Proc. 1997 IEEE Battery Conference on Applications and Advances*, pp. 163-170

[13] P. H. Chou, C. Park, J. Park, K. Pham, and J. Liu, "B#: a Battery Emulator and Power Profiling Instrument," *IEEE Design & Test of Computers*, vol. 22 (2), pp. 150-159, Mar.-April 2003

[14] L. Benini, A. Macii, E. Macii, and M. Poncino, "Discharge Current Steering for Battery Lifetime Optimization," *IEEE Trans. Computers*, vol. 52 (8), pp. 985-995, Aug. 2003

[15] Q. Wu, Q. Qiu, and M. Pedram, "An Interleaved Dual-Battery Power Supply for Battery Operated Electronics," *in Proc. 2000 IEEE Design Automation Conference*, pp.387-390

[16] D. W. Deesa, V. S. Battagliaa, and A. Belangerb, "Electrochemical modeling of lithium polymer batteries," *Journal of Power Sources*, 110, pp. 310–320, 2000

[17] L. Song and J. W. Evans, "Electrochemical-Thermal Model of Lithium Polymer Batteries," *Journal of The Electrochemical Society*, vol. 147 (6), pp. 2086-2095 , Feb. 2000

[18] M. Doyle, T. F. Fuller, and J. Newman, "Modeling of Galvanostatic Charge and Discharge of the Lithium/Polymer/Insertion Cell," *The Electrochemical Society*, vol. 140 (6), pp. 1526-1533, June 1993

[19] J. Newman, K. E. Thomas, H. Hafezi, and D. R. Wheeler, "Modeling of lithium-ion batteries," *Journal of Power Sources*, vol. 119 (121), pp. 838–843, 2003

[20] T. F. Fuller, M. Doyle, and J. Newman, "Simulation and Optimization of the Dual Lithium Ion Insertion Cell," *The Electrochemical Society*, vol. 141 (1), pp. 1-10, Jan. 1994

[21] J. Newman, K. E. Thomas-Alyea, "Electrochemical Systems," Third Edition. 2004

[22] Stephan Buller, Marc Thele, Rik W. A. A. De Doncker, and Eckhard Karden, "Impedance-Based Simulation Models of Supercapacitors and Li-Ion Batteries for Power Electronic Application," *IEEE Trans. Industry Applications*, vol. 41 (3), May/June 2005

[23] D. Rakhmatov, S. Vrudhula, and D. A. Wallach, "A Model for Battery Lifetime Analysis for Organizing Applications on a Pocket Computer," *IEEE Trans. Very Large Scale Integration (VLSI) Systems*, vol. 11 (6), pp. 1019-1030, Dec. 2003

[24] P. Rong and M. Pedram, "An Analytical Model for Predicting the Remaining Battery Capacity of Lithium-Ion Batteries," *IEEE Trans. Very Large Scale Integration (VLSI) Systems*, vol. 14 (5), pp. 441-451, May 2006

[25] C. Chiasserini and R. R. Rao, " Energy Efficient Battery Management," *IEEE Journal on Selected Areas in Communication*, vol. 19 (7), pp. 1235-1245, July 2001

[26] N. Mohan, T. Undeland and W. Robbins, "Power Electronics: Converters," Applications, and Design, 3rd Edition, John Wiley & Sons, Inc., 2003.

[27] A. Ostadi, "Optimal Sizing of Battery/Ultracapacitor-Based Energy Storage Systems in Electric Vehicles," Ph.D. dissertation, Dept. ECE., Univ. Waterloo, Waterloo, 2015.

[28] L. Wang and N. Ertugrul, "Selection of PI compensator parameters for VSC-HVDC system using decoupled control strategy," in *proc. 2010 Universities Power Engineering Conference (AUPEC)*,. pp. 1-7

[29] M. Rashid, "Power Electronics Handbook," 2nd ed., vol. 34. Elserier, 2007.

[30] A. Yazdani, R. Iravani, "Voltage-Sourced Converters in Power Systems : Modeling, Control, and Applications," 3rd ed., John Wiley & Sons, Inc., 2003

[31] Y. Gao, J. Li ; H. Liang, "Simulation of Three Phase Voltage Source PWM Rectifier," in 27-29 March 2012, *Power and Energy Engineering Conference (APPEEC)*,. pp.1-4.

[32] B. Kuo, "Automation Control System,"4th ed. Vol 6, Prentice-Hall, 1982.

[33] Li YaPing, Yang ShengChun, Wang Ke and Zeng Dan, "Research on PI controller tuning for VSC-HVDC system," in 16-20 Oct. 2011, *Advanced Power System Automation and Protection (APAP), 2011 International Conference* on, pp. 261 – 264.

[34] Ruan Yi and BoShi Chen, "Control Systems of Electrical Drives- Motion Control Systems," 4th ed., China Machine Press, 2010.

[35] M. Pape, “Design of a Flexible and Modular Test Bed for Studies on Islanded Microgrids,” M.A.Sc dissertation, Dept. ECE., Univ. Waterloo, Waterloo, 2015.